TROPICAL CYCLOGENESIS FACTORS IN A WARMING CLIMATE

A Thesis

by

STEPHEN CHRISTOPHER CATHEY

Submitted to the Office of Graduate Studies of
Texas A&M University
in partial fulfillment of the requirements for the degree of

MASTER OF SCIENCE

December 2011

Major Subject: Atmospheric Sciences

Tropical Cyclogenesis Factors in a Warming Climate

TROPICAL CYCLOGENESIS FACTORS IN A WARMING CLIMATE

A Thesis

by

STEPHEN CHRISTOPHER CATHEY

Submitted to the Office of Graduate Studies of
Texas A&M University
in partial fulfillment of the requirements for the degree of

MASTER OF SCIENCE

Approved by:

Chair of Committee,	Robert L. Korty
Committee Members,	Gerald R. North
	Steven M. Quiring
	Courtney Schumacher
Head of Department,	Kenneth P. Bowman

December 2011

Major Subject: Atmospheric Sciences

ABSTRACT

Tropical Cyclogenesis Factors in a Warming Climate. (December 2011)

Stephen Christopher Cathey, B.S., Texas A&M University; B.S., Texas Tech University

Chair of Advisory Committee: Dr. Robert L. Korty

Understanding the underlying causes of tropical cyclone formation is crucial to predicting tropical cyclone behavior in a warming environment, given the Earth's current warming trend. This study examines two sets of simulations from the National Center for Atmospheric Research (NCAR) Community Atmosphere Model version 3.1 (CAM3): one with aerosol forcings and one without. We looked at how four factors known to be important to tropical cyclone formation vary as carbon dioxde and the ensuing temperature changes increase to very high levels. These factors include Maximum Potential Intensity (MPI), mid-tropospheric moisture content, 200-850 mb vertical wind shear, and 850 mb absolute vorticity. We considered different representations of mid-tropospheric moisture by examining both relative humidity and χ, a non-dimensional measure of the saturation entropy deficit at 600 mb. We also looked at different combinations of these factors, including several variations of a Genesis Potential Index (GPI) and an incubation parameter, γ, that is related to the length of time required to saturate the middle troposphere and aid tropical cyclogenesis. Higher MPI, lower saturation deficits and higher relative humidity, lower wind shear, and higher

absolute vorticity all act to enhance the GPI and lower the incubation time, meaning larger environmental support for tropical cyclone development and intensification.

In areas where tropical cyclone development is prevalent today, we found that shear generally decreased, but MPI decreased, absolute vorticity decreased, and the saturation deficit increases. Thus, in today's prevalent tropical cyclone regions, conditions become less favorable for development and intensification as the climate warms. On the other hand, genesis regions tend to push northward into the subtropics, as conditions become much more favorable for development up to ~40°N due to both decreased wind shear and much higher MPI values.

ACKNOWLEDGEMENTS

I would like to thank my committee chair, Dr. Korty, and my committee members, Dr. Schumacher, Dr. North, and Dr. Quiring for their guidance and support throughout the course of this research.

Thanks also go to my friends and colleagues and the department faculty and staff for making my time at Texas A&M University a wonderful experience. I also want to extend a special thank you to Mr. Ryan Zamora, whose assistance with the data files was invaluable.

Finally, thanks to my mother and father for their love and support.

TABLE OF CONTENTS

LIST OF FIGURES

FIGURE Page

LIST OF TABLES

1. INTRODUCTION

Changes in climate can bring about potentially consequential results in tropical cyclone (TC) development (Emanuel et al., 2008). The conditions favorable for TC formation and development have been known for more than forty years (Gray 1968), and, although it is crucial to understanding how and why these conditions are important for TC climatology, only recently has attention returned to these questions (e.g., Emanuel and Nolan 2004; Camargo et al. 2007; Rappin et al. 2010; Tippett et al. 2011). Warmer temperatures in the tropics have been shown to increase power dissipation and intense TC frequency (Emanuel 2005; Webster et al. 2005), but there is also model evidence that the number of cyclones may simultaneously decline (Knutson et al. 2007; Knutson et al. 2010).

Maximum potential intensity (MPI) theory predicts that intensity limits will not be sensitive to sea surface temperatures (SSTs) alone, but rather to the relationship of SST to the thermodynamic structure of the atmosphere overhead (Emanuel 1986; Holland 1997). The laws of thermodynamics limit a TC's MPI, and this upper bound can be calculated from the large-scale fields that the models predict. MPI is set by the strength of fluxes from the sea to the atmosphere, and the thermodynamic stability of the atmospheric column overlying it (Bister and Emanuel 1998). Therefore, it is the relationship between the SST and the atmosphere above it that is important, not merely the absolute SST. For example, MPI changes very little in most of the Atlantic in

---

This thesis follows the style of *Journal of Climate.*

simulations of anthropogenic warming over the next fifty years, though this is not true in other basins despite a ubiquitous warming of SSTs (Vecchi and Soden, 2007b). Thus, it is of significant interest to understand how a changing climate may affect such TC factors, so that TC genesis and strength can be understood and predicted in a warmer climate. The goal of this research project is to examine how such environmental factors change in progressively warmer climates in different basins, and how regions conducive to the TC genesis change as well.

Large values of 200-850 mb wind shear are detrimental to TC genesis and intensification (Gray 1968; DeMaria 1996; Frank and Ritchie 2001; Rappin et al. 2010; Tang and Emanuel 2010). For surface pressure in an existing or developing TC to remain lower than its surroundings, the vortex must be anomalously warm throughout the troposphere (Gray 1968). Tropospheric vertical wind shear have been shown to have at least two distinct detrimental effects. First, large vertical wind shear produces a large ventilation of heat away from the TC. The condensational heat released by updrafts in the eyewall into the upper troposphere is advected in a different direction relative to the condensational heat released at lower levels. Thus, maintaining anomalously high temperatures throughout the troposphere in the vortex becomes much more difficult (Gray 1968; DeMaria 1996). Secondly, large vertical wind shear causes the vortex to tilt with height (DeMaria 1996; Frank and Ritchie 2001). This tilting results in a tilted potential vorticity (PV) pattern. For the TC to maintain its intensity, an increased midlevel temperature perturbation is required near the vortex center, reducing convective activity and inhibiting storm development (DeMaria 1996). Frank and Ritchie (2001)

alternatively theorize that wavenumber one asymmetries develop due to imbalances caused by shear that lead to upward motion and rainfall concentrated on the left side of the shear vector looking downshear, thus weakening the TC.

Convection is one ingredient necessary for a disturbance to develop into a TC (Gray 1968). Thus, low-level convergence is needed to have the necessary upward motion for thunderstorm development. TCs do not spontaneously arise from disorganized, random convection, but require an incipient vortex of sufficient strength around which the TC can organize (e.g., Nolan and Rappin 2008). Gray (1968) showed that condensational heating necessary to produce a net atmospheric warming in the vortex (thus making the vortex anomalously warm) can only be produced by vertical motion originating from levels below 900 mb. Gray also showed that low-level absolute vorticity plays the crucial role in establishing this low-level convergence necessary for convection formation.

We use output from a general circulation model run over a wide range of climate states to study the sensitivity of TC genesis factors to climate (see Section 3 for model details). A long, quality observational record for TCs does not exist. Until the satellite era, records are most likely incomplete (Landsea et al. 2006) due to the possibility of remote TCs being missed if no ship observations were near an existing TC. Even where records are long, their accuracy is suspect (Landsea et al. 2006). TC intensity is defined by the maximum sustained surface wind speed, and the main method for estimating TC intensity globally is the satellite-based pattern recognition technique called the Dvorak Technique (DT), which was invented in 1972, but was not applied routinely until the

early 1980s. Aircraft observations provide a direct measurement and have been available since the 1940s, but these are unavailable to fully monitor entire basins globally. Thus, the DT is mostly used, but this technique is not without flaws. First, the DT does not directly measure the maximum sustained surface wind, but rather uses pattern recognition to estimate TC strength. Secondly, the DT is subjective, and it is quite common for different forecasters to look at the same information and estimate the TC to have significantly different intensities (Landsea et al. 2006; Kossin 2008). The DT was first developed for visible imagery, so TC intensities could not be estimated at night, which limited the estimates of the maximum sustained surface wind speed. The IR method was published in 1984, based on the temperature contrast between the warm eye of the cyclone and the cold cloud tops of the eyewall, and provides a reasonably good estimate for maximum sustained surface wind speed. TC intensities using the DT were probably commonly underestimated in the 1970s and 1980s because there were only a few satellites, and they had low spatial resolution (Landsea et al. 2006). The pre-1990 TC data for all basins are full of large uncertainties, gaps, and biases. Trend analyses for extreme TCs may be spurious due to operational changes that have resulted in more intense TCs being recorded (Landsea et al. 2006). The best current dataset, HURDAT, includes a mix of subjective estimates of intensity with some limited actual measurements, but which observation belongs to which set is undocumented. Thus, an objective look at synthetic climates states is necessary until the data sets become more homogeneous, complete, and a much longer record exists.

This goal of this thesis is to see how the environments that spawn TCs will change. This is a multi-faceted question: how do factors favorable for genesis change in the regions that produce storms today, and do regions presently inhospitable become conducive? Figure 1 shows the genesis locations of every TC between 1970 and 2008 (data were taken from the best track data, HURDAT, and are available from NOAA's website; see also Powell et al. 1998). In the Northern Hemisphere, two prominent areas produce the bulk of observed storms: a region that stretches from Africa across the tropical Atlantic, Caribbean Sea, and Gulf of Mexico into the Eastern Pacific; and a second cluster in the Pacific Ocean west of the dateline.

These regions are marked by boxes outlined in red (Western Pacific), blue (Eastern Pacific), and green (Atlantic) in Figure 1. (A third belt from the Indian Ocean into the southwest Pacific produces nearly all storms that form in the Southern Hemisphere today. Our analysis is restricted to the Northern Hemisphere in this thesis.) The region bounded between 5° and 25°N and 100°E to the dateline defines the Western Pacific. The region between 8° and 20°N east of 125°W to the coast defines the Eastern Pacific. The tropical Atlantic box is defined to include the band of latitudes between 8° and 20°N west of 20°W (commonly referred to as the "main development region") and the area south of 33.5°N west of 60°W. The precise boundaries are somewhat arbitrary, but as the areas enclosed are the regions in which storm formation is common today, we are particularly interested in how genesis factors evolve here. In subsequent figures, analysis that is confined to one of these three regions corresponds to the area shown in

the boxes. We also investigate how variables change in the remainder of the tropics, including those areas inhospitable to storm formation in today's world.

2. PREVIOUS WORK

Attempts have been made to quantifiably relate TC genesis to environmental factors of development over the past few decades. Gray (1979) identified 6 main environmental factors that influence TC genesis: low-level vorticity, the Coriolis parameter, vertical wind shear, sea surface temperatures (SSTs) greater than twenty-six degrees Celsius with a deep thermocline, deep conditional instability, and low-to-mid level relative humidity (RH). Subsequent development of potential intensity theory shows that the role of SST and deep conditional instability are fundamentally coupled, and so the combined metric has more direct relevance than either do separately (Emanuel 1986, 1988; Holland 1997; Bister and Emanuel 2002). Absolute vorticity, the sum of relative vorticity (i.e., low-level vorticity) and the Coriolis parameter, provides incipient rotation around which convective systems can begin to organize. Emanuel and Nolan (2004) developed an empirical index based on these updated four parameters, and called it the genesis potential index (GPI):

$$GPI = \left|10^5 \eta\right|^{3/2} \left(\frac{H}{50}\right)^3 \left(\frac{V_{pot}}{70}\right)^3 \left(1 + 0.1 V_{shear}\right)^{-2} \quad (1)$$

where η is the 850 mb absolute vorticity (s^{-1}), H is the 600 mb relative humidity (%), V_{pot} is the maximum potential intensity (m/s), and V_{shear} is the magnitude of the 200-850 mb wind shear vector (m/s).

Emanuel et al. (2008) argues that another representation of low-mid level moisture is necessary for studies of changing climates, specifically, the normalized

difference between the moist entropies of the boundary layer and mid-troposphere. Dry air in the middle troposphere prevents the supply of low-level, moist (high entropy) air. Mixed with wind shear, the lack of moist, low-level air influx can prevent a TC from forming (Tang and Emanuel 2010). This difference, also called the saturation deficit, χ, is a measure of the moist entropy deficit of the middle troposphere: the larger value that χ has, the drier the troposphere is. This produced a second empirical derivation of the GPI (Emanuel 2010):

$$GPI = |\eta|^3 (\chi)^{-\frac{4}{3}} MAX((V_{pot} - 35),0)^2 (25 + V_{shear})^{-4} \quad (2)$$

where the specific definition of χ is:

$$\chi = \frac{S_m^* - S_m}{S_o^* - S_b} \quad (3)$$

and S_m and S_b are the entropies at 600 mb and the boundary layer, respectively, and S_m^* and S_o^* are the saturation moist entropies at 600 mb and the surface, respectively. This second GPI equation was designed with two improvements in mind. First, the equation was specifically designed to have units of a genesis metric, which is number of events per unit area per unit time. Secondly, the equation incorporates a non-climate specific dependence on mid-level moisture. To see why χ offers a measure of mid-level moisture that evolves with climate, consider the following.

The entropy S and saturation entropy S^* are defined:

$$S = c_p \ln \theta_e \quad (4)$$

$$S^* = c_p \ln \theta_e^* \quad (5)$$

where c_p is the heat capacity for constant pressure, and θ_e and θ_e* are the equivalent potential temperature, and saturation equivalent potential temperature, respectively. These are defined:

$$\theta_e = \theta \exp\left(\frac{L_v r}{c_p T}\right) \tag{6}$$

$$\theta_e^* = \theta \exp\left(\frac{L_v r^*}{c_p T}\right) \tag{7}$$

where θ is the potential temperature, L_v is the latent heat of vaporization, T is the temperature at the lifting condensation level (LCL), and r and r* are the mixing ratio and saturation mixing ratio, respectively. Equation (6) can be approximated by (Bohren and Albrecht 1998, p. 294):

$$\theta_e = \theta + \frac{L_v r}{c_p} \tag{8}$$

and (7) can be approximated by:

$$\theta_e^* = \theta + \frac{L_v r^*}{c_p} \tag{9}$$

Thus, taking the difference of (4) and (5), it can be shown that:

$$S^* - S = c_p\left(\ln\theta_e^* - \ln\theta_e\right) \tag{10}$$

and substituting (8) and (9) and simplifying gives the approximation:

$$S^* - S \approx \frac{L_v\left(r^* - r\right)}{T} \approx \frac{L_v\left(q^* - q\right)}{T} \tag{11}$$

where q and q* are the specific humidity and the saturation specific humidity, respectively, and the last approximation is valid because $r << 1$ (see also Eqn. 17). As

climate warms, if RH remains fixed, $S^* - S$ increases as both q^* and S are functions of temperature too. Thus, an entropy deficit is proportional to the saturation deficit.

We define wind shear to be the magnitude of the difference between the wind vectors on the 850 and 200 mb surfaces:

$$V_{shear} = \sqrt{\left(u_{200} - u_{850}\right)^2 + \left(v_{200} - v_{850}\right)^2} \tag{12}$$

where u_{200} and u_{850} are the zonal components of the wind at 200 and 850 mb, respectively, and v_{200} and v_{850} are the meridional components of the wind at 200 and 850 mb, respectively. Gray (1968) showed that increased wind shear led to ventilation of the upper air heat anomaly present (and necessary) for TCs to form, persist, or strengthen, thus preventing genesis or weakening TCs. Frank and Ritchie (2001) theorized that wavenumber one asymmetries cause the vortex to tilt, inhibiting development.

Absolute vorticity was calculated as follows (Holton 2004, p. 92):

$$\eta = \zeta + f \tag{13}$$

where ζ is the vertical component of the relative vorticity vector, the third term of the curl of the wind vector, specifically defined as:

$$\zeta = \frac{\partial v}{\partial x} - \frac{\partial u}{\partial y} \tag{14}$$

and

$$f = 2\Omega \sin\phi \tag{15}$$

where f is the Coriolis parameter, $\Omega = 7.292 \times 10^{-5}$ rad s^{-1} is the angular speed of rotation of the earth, and ϕ is the latitude in radians. Gray (1968) showed that positive

absolute vorticity produces synoptic low-level convergence in the Northern Hemisphere, producing thunderstorms needed for TC development.

RH, denoted H, is calculated at the 600 mb level as follows:

$$H = \frac{r}{r_s} \tag{16}$$

where r is the mixing ratio, which is related to specific humidity q by:

$$r = \frac{q}{1-q} \tag{17}$$

and r_s is the saturation mixing ratio defined as:

$$r_s = \frac{R_d}{R_v}\left[\frac{e_s}{\left(p + e_s\right)}\right] \tag{18}$$

where R_d is the gas constant for dry air, and R_v is the gas constant for water vapor, p is the total pressure (600 mb), and e_s is the saturation vapor pressure.

MPI was first derived by Emanuel (1986), using a Carnot heat engine cycle model for a TC in which energy is added at the warmer ocean surface and lost in the cooler outflow. Emanuel argued that the upper bound on the intensity of a hurricane is determined by the product of the maximum possible heat input from the ocean to the atmosphere and the thermodynamic efficiency proportional to the temperature difference between the sea surface and lower stratosphere (Emanuel 1988, 1991). Emanuel (2003) presented an alternate derivation of MPI using the First Law of Thermodynamics. It begins by quantifying the flux of momentum into the sea and flux of enthalpy from the sea using the bulk formulas:

$$F_m = -C_D \rho |V| V \tag{19}$$

$$F_k = C_k \rho |V| \left(k_0^* - k \right) \tag{20}$$

where V is the near-surface wind speed, ρ is the air density, k is the specific enthalpy of air near the surface, k_o^* is the saturation enthalpy at the temperature of the ocean surface, C_D is the transfer coefficient of momentum fluxes (i.e., the drag coefficient), and C_k is the transfer coefficient of enthalpy fluxes. The vertically integrated dissipative heating of the atmospheric boundary layer is given from Bister and Emanuel (1998) as:

$$D = C_D \rho |V|^3 \tag{21}$$

Taking the surface temperature to be T_s and the outflow temperature to be T_o, then, by the Carnot theorem, the net production of mechanical energy in the cycle is

$$P = 2\pi \frac{T_s - T_o}{T_o} \int_a^b \left[C_k \rho |V| \left(k_o^* - k \right) + C_D \rho |V|^3 \right] r dr \tag{22}$$

where the integral is taken over the first leg of the cycle. The net energy dissipation is

$$D = 2\pi \int_a^b C_D \rho |V|^3 r dr \tag{23}$$

Assuming the integrals in (22) and (23) are dominated by their integrands near the radius of maximum wind speed, equating (22) and (23) yields an expression for the maximum wind speed (MPI):

$$|V_{\max}|^2 = \frac{C_k}{C_D} \frac{T_s - T_o}{T_o} \left(k_o^* - k \right) \tag{24}$$

3. MODEL DATA

We examine the response of TC genesis factors in two series of experiments run using the National Center for Atmospheric Research (NCAR) Community Atmosphere Model version 3.1 (CAM3) coupled to a slab ocean model with prescribed present-day ocean heat transport (OHT) values. The runs in each series of experiments differ only in the loads of carbon dioxide they carry; the simulations we study here cover a very wide range of increasingly high loads (280 ppm to 8960 ppm), which offers us an opportunity to examine the behavior of TC genesis factors in climates that go far beyond a mere linear perturbation to the present-day world. Table 1 offers an overview of some salient features.

Matthew Huber ran the simulations prior to this study, and analysis of their output continues to yield a number of results revealing model behavior in extreme climate states in addition to applications to past hot climates, such as those of the early Cenozoic when the planet was ice free and hot (e.g., Caballero and Huber 2010; Sherwood and Huber 2010; Speelman et al. 2010; Williams et al. 2009; Abbot et al. 2009). The simulations have T42 spectral resolution and their output was gridded to a regular ~2.8° by 2.8° latitude-longitude grid. All simulations were run to equilibrium, and our analysis was based on averages over all available equilibrated output, varying between 15 and 31 years of data by case (see Table 1). Additional description of the model simulations can be found in Caballero and Huber (2010) and Williams et al. (2009).

Figure 2 shows the average surface temperature averaged over all Augusts, Septembers, and Octobers in the Northern Hemisphere of three simulations with increasingly large loads of carbon dioxide: (a) one with present-day (i.e., 1990) levels (355 ppm; PD; control), (b) a simulation with 8 times more CO2 than the pre-industrial atmosphere (2240 ppm; PD3), and (c) a simulation with 32 times more CO2 than the pre-industrial era (8960 ppm; PD5). (Further description of these specific runs is provided below.) Surface temperatures are generally ~5°C higher throughout the tropics in the PD3 simulation than in the control and ~15°C higher in PD5. (Here, we give a fixed, latitudinal definition of the tropics, being between 5°N and 30°N.) Hence, this series of simulations offers an opportunity to explore how TC genesis factors evolve over a range of climate far wider than that previously explored. While no data exist to verify the model predicted behavior at these extreme states, it is helpful to know how the computer models tasked with predicting changes over the next century behave over a wider range of parameters.

We examine two sets of experiments that overlap extensively but offer distinct parameter values for each series. The first is run using a preindustrial-era solar constant of 1365 W/m2 without any aerosol forcing; the second has a present-day solar constant of 1367 W/m2 and includes aerosol forcings. Set 1, which we refer to as "UH" for ultra-hot includes 6 cases with different levels of carbon dioxide: (1) preindustrial (PI) era levels of 280 ppm; (2) 560 ppm, which is double the PI era levels; (3) 1120 ppm, quadruple the PI levels; (4) 2240 ppm, an eight-fold increase; (5) 4480 ppm, a sixteen-fold increase; and (6) 8960 ppm, thirty-two times more than during PI. The second set,

which we refer to as “PD” for the present-day parameter choices, is similarly structured but with three cases using different amounts of carbon dioxide: (1) a 1990 level of 355 ppm, (2) one with 2240 ppm, and (3) one with 8960 ppm. The PD3 and PD5 cases are similar but slightly cooler than their UH3 and UH5 counterparts, as they (the PD cases) include aerosol forcings that the UH series does not. PD3 produces temperatures between those in UH2 and UH3, and so represents a hot climate in the middle of the range we examine. PD5 is similar to the UH5 case and represents the hot extreme of our study.

The UH series offers five cases that progressively double carbon dioxide levels to increasingly large values. (Because the temperature response to increasing carbon dioxide is logarithmic, this experimental design offers a set of experiments in which a steady, quasi-linear temperature rise continues across the set.) CCSM3 has a climate sensitivity somewhat lower than other models developed at peer institutions; if the climate sensitivity of the model were higher, the temperatures in each case would have been achieved with lower levels of carbon dioxide. Hence the values of carbon dioxide act as the knob for dialing up the heat.

Each of the series offers a unique set of advantages and drawbacks. The second series (PD) offers a realistic present-day control run, but presents fewer cases for direct comparison. The UH series samples more parameter space (it was developed originally as a control for yet another series with Eocene epoch geography), but the slab ocean with ocean heat transport (OHT) prescribed at present-day values limits the utility of the control, preindustrial era case.

Because the preindustrial case, which has 280 ppm CO2, is colder than the present-day climate, the model evacuates laterally more heat from the equatorial Pacific than surface fluxes are able to maintain. Examining the mixed layer heat budget of a slab ocean reveals the problem:

$$c_p \frac{\partial T}{\partial t} = F_s - F_{OHT} \tag{25}$$

Temperatures (T) change with time owing to heat fluxes across the ocean surface (Fs) and lateral transport out of the box (FOHT), which here is prescribed. While this set up offers a new layer of freedom that prescribing SSTs precludes, it also presents a challenge in any climate colder than the one for which the OHT values were derived. If OHT is prescribed to be stronger than they would be in the alternate climate, then surface fluxes from the atmosphere are solely responsible for maintaining an equilibrium SST. But if the atmosphere is colder than the climate for which OHT was fixed, it may be unable to supply sufficient heat fluxes. Hence a drain begins and equatorial SSTs where the OHT is too strong fall until the code orders it stopped (usually at the point sea ice would form). This unfortunate problem is a common and well-known artifact of slab ocean models for such states (e.g., Barreiro 2011), but these types of simulations continue to provide useful information, even though they introduce a level of nuance to interpreting the results. Given that the tropical Pacific has a physically unrealistic cold tongue along the equator, we exclude this case from analysis and focus instead on how the very hot simulations in the UH series differ from the doubled-carbon dioxide experiment. It should be noted that the limitation of using fixed OHT is far less severe in climates hotter than that from which the OHT was taken, which is our focus here. If

OHT is too weak, then the balance of surface fluxes may return a spurious amount to the atmosphere, but the model is free to take this away by running with long term top-of-atmosphere fluxes that do not balance.

The model output includes temperature (T), winds (u and v components of the horizontal wind vector V) and specific humidity (q) every six hours. We computed daily averages of each variable and then computed daily values of the genesis factors. Monthly averages were then calculated from these daily values and then long-term climatologies were produced from these. Later experience taught us that these values could be computed directly from long-term mean climatologies without loss of information (S. Camargo 2011, personal communication), so the genesis factors from the PD series were computed from monthly-averaged fields without using the daily output. We use this series principally to summarize the main findings, as the 2240 and 8960 ppm CO2 simulations of the PD series differ from their counterparts in the UH batch mainly by mitigating warming of the North Atlantic via the inclusion of aerosol forcing in the PD series; they are otherwise broadly similar.

4. GENESIS FACTORS

4.1. Maximum potential intensity

Since its development a quarter century ago (Emanuel, 1986), maximum potential intensity (MPI) has proven to be a central metric for evaluating the thermodynamic environment in which TCs live. It is the upper limit of intensity that the laws of thermodynamics will allow: operating with the efficiency of a Carnot heat engine, the sea surface serves as the hot reservoir and the temperature at the level of convective outflow serves as the cold reservoir. The structure of the atmosphere places a lower limit on the cold reservoir, essentially that of the tropical tropopause (temperatures rise in the stratosphere above this level). MPI has proven more useful still: while many things limit an actual storm from reaching this speed limit (i.e., mixing cold water to the surface of the ocean, wind shear, dry air intrusions; see Emanuel et al. 2004), intensity nonetheless scales with MPI, yielding an almost linear cumulative probability distribution (Emanuel 2000). (That is, the actual intensity of any storm at any time has an almost equal probability of being any fraction of the local MPI.) Moreover, while many early observational studies noted that storms almost always form over water 26°C or warmer (Palmen 1948; Gray 1968), this is coincidental, not causal. This isotherm roughly bounds the regions of high MPI today as it is generally collocated near the edge of the tropical atmosphere where trade inversions cap deep convection (K. Emanuel 2010, personal communication). As we show below, any SST regarded as a threshold for TC activity varies itself with climate.

Figure 3 shows the August-October mean MPI for (a) the 1990 level PD, (b) the 2240 ppm PD3 case, and (c) the very hot 8960 ppm PD5 case. While MPI falls off rapidly in PD outside the regions where storms form today (the most active locations, shown in Figure 1, are boxed here too), the regions of high MPI expand poleward slightly in PD3 and significantly in PD5. This indicates that conditions at the subtropical edge of the regions that spawn most storms today has become thermodynamically more conducive for TCs and their associated deep convection. This is consistent with a poleward expansion of the Hadley circulation, which has appeared in numerous studies of warmer climates (Frierson et al. 2007; Hu and Fu 2007; Seidel and Randel 2007; Seidel et al. 2008; Lu et al. 2007; Seager et al. 2007; Korty and Schneider 2008). Additionally, the hottest cases (PD5 and UH5) are radically different from all others in that they have equatorial superrotation (Caballero and Huber 2010) and appear to sustain deep convection throughout the year over middle latitude oceans (R. Zamora 2011, personal communication).

The annual cycle of MPI by case is shown in Figure 4. There is a steady upward trend in all regions of the tropics with warming, though cases UH1, UH2, and UH3 are fairly close together, UH4 has a larger increase, and the UH5 case is much higher than the other cases (though in the western Pacific, the UH5 case has decreased in MPI significantly). The UH5 case has high MPI in the Northern Hemisphere tropics during the entire year, which is consistent with the findings noted above that extratropical deep convection continues through the winter months of these simulations. (The shortcomings of the UH0 case are also apparent in the Eastern Pacific: because SSTs are

unrealistically cold along the eastern equatorial Pacific owing to fixed OHT, MPI falls to near zero during summer months here.)

The change in MPI between cases is instructive, and Figure 5 shows the difference between (a) PD3 and PD and (b) PD5 and PD. First note that MPI has generally increased significantly just poleward of the regions that spawn storms today (throughout the subtropical Pacific and western North Atlantic, but not in the central and east Atlantic, nor the east Pacific in the PD3 case). This is the poleward expansion of high MPI noted above. But within the regions that support storm formation today, a more complex pattern is seen. While MPI increases in some areas, it decreases in others. Note that the drop is particularly high in the central Pacific in PD5, where some values have fallen by more than 10 m/s, despite the fact that SSTs are well above 40°C (Figure 2c).

To gain further insight into these changes, we plotted the change in MPI overtop changes in SST, which are shown in Figure 6. Note that while every location is significantly warmer in both cases, some areas have warmed by much larger amounts than others. Generally speaking, those areas where temperatures increased the most saw MPI rise, while those that warmed least saw it drop. This is shown more clearly in Figure 7, which reveals a remarkable correlation between the changes in SST and changes in MPI throughout the tropics (the correlation coefficient for the best-fit line through all tropical points is $R = 0.91$ for PD3-PD and $R = 0.94$ for PD5-PD).

Vecchi and Soden (2007b) argued that remote changes in SST were more important than the local absolute SST to MPI. Essentially, where SSTs are relatively

hottest (the greatest values above a tropical average), MPI values are high. Where SSTs are relatively cold, MPI values are low. This holds so long as variations in the marine boundary layer are large while variations in the middle and upper troposphere are comparatively small. They argue that remote SST temperatures can influence MPI through their influence on upper tropospheric temperatures (T_o in Eqn. 24). In the tropical free troposphere, the Coriolis force is weak, temperature gradients are small, and upper tropospheric temperature anomalies are determined by changes in the mean tropical SST. They found that in a warming climate, despite local SSTs increasing steadily, MPI showed large decadal variability. Thus, remote changes in SST become more important.

The full suite of experiments is summarized in Figure 8, which shows the joint distribution of SST and MPI. As the climate simulations get progressively hotter, the regions of significant MPI shift to progressively warmer temperatures. The center of gravity of each cluster shifts also to higher MPI through the UH3 case, after which it levels off and slowly subsides. Figure 9 shows that there is a continuous elevation of the equilibrium level of neutral buoyancy (the top of the positive area of convective available potential energy (CAPE) in a sounding). By UH5, the LNB is commonly 50 mb, an altitude of ~20 km in today's atmosphere. The tropopause rises in these hottest simulations (Caballero and Huber 2010), as deep convection above an ocean >40°C penetrates to altitudes much higher than observed in the present-day climate. But with the steady rise in the height of deep convection, why do MPI values saturate at values below 100 m/s? Figure 10 suggests it is because the temperature of the tropopause

begins to rise with the UH3 simulation. Although the surface temperature continues to rise through the very hot simulations, so too does the entire column above it, and the difference between SST and outflow temperature, on which the thermodynamic efficiency of a TC is built, no longer grows as climate warms past the 2240 ppm simulation.

4.2. Mid-tropospheric moisture content

In the present climate, seasonal and spatial variations of saturation entropy deficits s* - s are dominated by variations in relative humidity (RH; see Eqn. 11). However, in other climates where the mean temperature changes, saturation entropy deficits are affected by changes to the specific saturation humidity q*, whereas RH stays relatively constant (Emanuel et al. 2008). Thus, RH can no longer be used as a proxy for saturation deficits in different climates, as both it and temperature affect the size of the deficit.

The non-dimensional number χ measures the relative importance of subsidence across the boundary-layer top as compared to the effect of surface fluxes on the boundary layer entropy. Larger values of $S_m - S_m^*$ (from Eqn. 3) mean greater sub-saturated mid-levels require relatively longer incubation periods for convection to moisten the mid-troposphere, which implies that the detrimental low-entropy convective downdrafts continue for relatively longer periods of time during the genesis window (Emanuel 2008; Rappin et al. 2010). Likewise, a decrease in $S_o^* - S_b$ indicates a reduction in ocean-to-air fluxes, diminishing boundary layer support for convective

inflow (Rappin et al. 2010). Therefore, higher values of χ indicate an increasingly inhospitable environment for TC development (through reduced surface fluxes, a dry middle troposphere, or some combination of both).

Figure 11 shows 600 mb RH for the (a) PD, (b) PD3, and (c) PD5 cases. The Intertropical Convergence Zone can easily be seen between ~5-8°N, as RH values peak there. Likewise, the effect of the descending branch of the Hadley cell can be seen in the subtropics regions around 30°N, with very low RHs in this region. The RH in the tropics remains fairly constant over these cases. Over the subtropics, the 600 mb level moistens, though over both the northeastern Pacific and the northeastern Atlantic, the RHs are still too low to help TC genesis (RH > 50% is necessary, based on Eqn. 1). However, in the western Pacific, RH increases dramatically and becomes high enough by PD5 to support TC genesis/intensification. This is verified by looking at Figure 12. From PD to PD3, the subtropical Pacific relative humidity increases by about 2-8% with the exception of the central Pacific, and the tropical RH decreases by about 5-15%. Nearly all of the Atlantic basin has lower RH, especially the southwestern North Atlantic and the Caribbean. However, progressing from a PD to the PD5 case, the trends seen previously in Figure 11 are all seen here. In the main development regions, Figures 11 and 12 suggest a southward progression of the ITCZ. The cold tongue persistent in the equatorial east Pacific in today's climate warms more as the climate warms more than the surrounding Pacific waters, as seen in Figure 13. This leads to more homogenous SSTs in the eastern Pacific, allowing the ITCZ to drift southward to its more natural near-Equatorial position.

Figure 14 shows χ for the (a) PD, (b) PD3, and (c) PD5 cases. Values throughout all of the basins increase with a warming climate. χ increases a bit more in the central and northeast Atlantic than the rest of the basin, but the difference is minimal. Figures 15 and 16 show the seasonality of both RH and χ, respectively. RH peaks in all of the tropics, as well as the sub-basins, in the warmest months of July through October, and has a minimum in late winter to early spring. This coincides with χ having a peak in the late winter to early spring, and a minimum in the warmest months.

Another aspect of Figures 15 and 16 are the differences between the cases in each basin. Both in the northern hemisphere tropics and west Pacific, RH increases with warming climates. However, in the east Pacific and the Atlantic, RH tends to have a negative correlation with warming climates, i.e., RH goes down with an increase in temperature. For χ, a warming climate leads to a higher value of χ, though in the west Pacific, the differences between the cases are minimal compared to the other basins.

Figure 17 relates RH and χ by showing the saturation entropy difference as a function of both RH and temperature. In warmer climates, the amount of water vapor that can be present in the atmosphere increases exponentially with a corresponding linear increase in temperature. Thus, more water vapor is present in the atmosphere at warmer temperatures as well. However, Figure 17 shows that at a constant RH, increasing temperature leads to an exponential increase in saturation entropy deficit. From Eqn. 11, an exponential increase in saturation entropy deficit leads to a corresponding exponential increase in saturation moisture deficit. Thus, since RH levels change little with respect to differing climates, the moisture deficit will increase exponentially with a warming

climate, and thus is a detriment to TC genesis. A higher value of χ is detrimental for TC genesis and development, based on (2). Therefore, both RH and χ show increasing saturation deficits throughout the basins, and in either case, lower GPI values. Thus, despite there being more moisture available in a warmer climate, due to the larger saturation deficit, TC genesis will be hampered.

4.3. Wind shear

As shown in Section 2, for both thermodynamic and dynamic reasons, vertical wind shear is detrimental to TC genesis and intensification (Gray, 1968; DeMaria, 1996; Frank and Ritchie, 2001; Rappin et al., 2010; Tang and Emanuel, 2010). Ventilation of heat and dry air entrainment are thermodynamic reasons, while tilting of the PV field and wavenumber one asymmetries are dynamic reasons for shear weakening the TC.

Because the actual large-scale wind field is nearly geostrophically balanced and the atmosphere is approximately hydrostatic, the vertical wind shear is related to the horizontal temperature gradient between any two pressure levels p_1 and p_2 by the thermal wind equation:

$$\left(\overrightarrow{V_g}\right)_2 - \left(\overrightarrow{V_g}\right)_1 = \left(\frac{R}{f}\ln\frac{p_1}{p_2}\right)\hat{k} \times \nabla\left(T_{avg}\right) \tag{26}$$

where $(\mathbf{V}_g)_2$ and $(\mathbf{V}_g)_1$ are the geostrophic wind vectors at pressure levels p_2 and p_1, respectively, R is the gas constant for dry air, f is the Coriolis parameter (Eqn. 15), and T_{avg} is the mean temperature of the layer of atmosphere between the two pressure levels (Wallace and Hobbs, 2006, p. 284). The larger the horizontal temperature gradient over

a specified area, the larger the magnitude of the geostrophic wind shear. Looking back at Figure 2, a decrease in the temperature gradient is evident throughout both the Pacific and Atlantic basins, especially within the boxes, meaning decreased wind shear throughout the domain. Figure 18 shows wind shear for the (a) PD, (b) PD3, and (c) PD5 warming scenarios. As a general trend, wind shear decreases with a warming climate, though that doesn't hold true in all areas. In the two Pacific boxes, shear decreases from PD to PD3, but increases from PD3 to PD5. In the Atlantic box, there is little to no change in most areas from PD to PD3, but decreased wind shear throughout the basin from PD to PD5. Figure 19 demonstrates these trends, with decreases in wind shear throughout both basins, with the sole exceptions being the extreme northeast Atlantic, and the central Pacific. Figure 20 shows the seasonal variability of wind shear in the boxes defined previously. For the most part, all of the cases, with the exception of the UH0 case, remain tightly grouped together, meaning wind shear doesn't change much between the differing climates. In the Atlantic, the warmer cases have lower average wind shears than the cooler cases between October and February. Since this area is fixed in space, the influence of mid-latitude systems beginning to affect the northern regions is seen here. The Atlantic box includes a region further north than the other boxes, so as mid-latitude systems move further southward as summer moves into fall and winter, the temperature gradient increases, and thus, wind shear increases there. As viewed with the GPI equation, this decrease in shear leads to an increase in the GPI.

4.4. Vorticity

Both observations and experience with numerical models have shown that TC genesis does not arise spontaneously from random convection, but is akin to a finite amplitude instability that requires an incipient vortex (a "seed") around which convection organizes (e.g., Emanuel 1989; Nolan and Rappin 2008; Dunkerton et al., 2009; Nolan 2011). Nevertheless it is not entirely clear at what point the supply of pre-existing vorticity switches from being rate-limiting to ample, and its magnitude has been included in genesis indices. More recently Tippett et al. (2011) found that by modifying the role of absolute vorticity in the genesis indices so that it saturates at some level improved the performance of the indices against observations (i.e., small amounts of cyclonic vorticity reduce the genesis potential, but large amounts no longer increase it). Whatever its precise role in different climates, we present and analyze the changes to this variable here, as it is important to understand how it affects the genesis indices examined in the next section.

Figure 21 shows the spatial distribution of the relative vorticity. As expected, relative vorticity is highest in the boxed areas, which outline the regions where most present-day hurricanes form (positive values indicate cyclonic flow in the Northern Hemisphere). The quasi-permanent Azores/Bermuda and North Pacific Highs are seen here with high negative values of relative vorticity (anti-cyclonic flow), from about 25°N to 45°N in both the Atlantic and Pacific basins, respectively. As the climate progresses from PD to PD3 to PD5, the magnitude of relative vorticity (regardless of the sign) decreases as the climate warms, consistent with a weakening of the tropical

circulation (Vecchi and Soden 2007a) The seasonal cycle is shown in Figure 22 and the same trend can be seen there as well. There is a maximum that occurs in all basins in September and October, and a minimum in the late winter months. In the entire northern hemisphere tropics, on average for most months, there is anti-cyclonic flow. However, this becomes near zero, or even cyclonic during September and October. In the boxed basins, as previously defined, there are larger amplitudes of maximums and minimums.

The decrease in magnitude of relative vorticity in a warming climate in the Atlantic MDR occurs concurrently with a decrease in the intensity of the African Easterly Jet (AEJ). Figure 23 shows the 700mb zonal winds, and a decrease in the AEJ (in addition to winds throughout the tropics, generally) decrease in magnitude. This decrease in the AEJ is consistent with a decrease in the temperature gradient, by thermal wind arguments. Burpee (1972) found that the AEJ is caused in response to the baroclinic zone between the hot and dry Sahara Desert, and the cooler, moist Atlantic. South of this jet is a region where the mean zonal flow is unstable. In this unstable region, horizontal and vertical shears are large and thus are sources of energy for the barotropic and baroclinic instabilities known as African Easterly waves, (AEW) the source of vorticity in the Atlantic tropical regions (Burpee, 1972). AEWs can be seen in climate models fairly well, though the amplitude and pattern of the AEWs is quite variable between different models and is highly dependent upon the physical parameterizations adopted. On an intra-seasonal to interannual time scale, AEWs are weakly affected by the horizontal and vertical resolution (Ruti and Aquila 2010).

As the climate warms the intensity of the easterly jet diminishes (Figure 23) and shifts slightly north. The integral constraints derived by Charney and Stern (1962) provide necessary conditions that must be met in order for baroclinic instabilities to exist. One way the constraint can be satisfied is for the meridional gradient of the mean-state quasi-geostrophic potential vorticity to change signs somewhere in the fluid. This derivative is plotted in Figure 24 for the profile along the prime meridian (it is computed from a time-mean background state using August-October climatology). While the necessary condition for instability is met in all three cases, the amplitude diminishes and shifts northward as the climate warms. Thus, the supply of additional incipient vorticity appears to decline in the hotter states, but this may yet turn out to be inconsequential. In very hot states, radiative-convective equilibrium simulations indicate that random convection may be able to self-organize (Nolan and Rappin 2007). Moreover, even if some level of vorticity remains necessary for cyclogenesis, this quantity does not appear to be rate-limiting poleward of 15° latitude in the present atmosphere (Tippet et al. 2011).

5. COMBINED METRICS

In the previous section we examined how four different TC genesis factors change over the range of climate simulations studied in this thesis. They showed a complex evolution: as temperatures first rise from today's levels, the highest maximum potential intensities increase slightly but level off after about three doublings of CO_2 and even decline slightly from their peaks in the very hottest simulation (see Figure 3). But the area of significant potential intensities expands poleward with a widening Hadley circulation, and much of the middle latitude oceans have nontrivial values in the hottest state. Shear in the tropics generally declines in magnitude as the climate warms, but changes are mixed in some smaller regions where storms are concentrated today. Yet on the other hand the saturation deficit steadily grows with temperature, leaving developing storms more vulnerable to mid-level entrainment of increasingly relatively dry air. How these offsetting changes would combine together to affect the environment is not easy to answer without actual observations of storms from such climates, but we examine metrics that have proven useful in capturing the inter- and intra-annual variability and regional differences in genesis in models of the present climate (e.g., Camargo et al. 2007). Additionally, recent theoretical progress provides a firmer foundation for why these particular variables are relevant to genesis (Tang, 2010; Tang and Emanuel, 2010; Rappin et al., 2010; Nolan 2011).

5.1. Incubation parameter and ventilation index γ.

Absent any shear, radiative convective equilibrium (RCE) models show that surface fluxes increase with temperature and can increasingly quickly saturate the mid-troposphere (Nolan et al., 2007). But once shear is present, no matter how small, the situation degrades with climate: Nolan and Rappin (2008) found that the same models became *less* favorable for genesis in warming climates in the presence of a constant shear. The reason is thermodynamic: shear advects environmental air into the saturated core of a hurricane, and as relative humidity is approximately unchanged with increasing SSTs in RCE models, the absolute saturation deficit grows with the saturation specific humidity. Hence, any finite amount of shear advects this dry air into a storm's core. While stronger surface fluxes could in principle overcome the larger midlevel deficits, in practice the surface fluxes do not grow as rapidly as the midlevel deficits, rendering warmer environments with fixed shear increasingly hostile to development. (Tropical boundary layers have higher relative humidity than do middle levels of the tropical troposphere. So for any given temperature increase, the saturation deficit grows faster in the mid-troposphere where the relative dryness is higher than in the marine boundary layer.)

But as we showed in the previous section, the shear itself can change too. Rappin et al. (2010) identified a non-dimensional parameter that combines shear, saturation deficits, and potential intensities to capture the time it takes for a system to develop across a range of climate states in RCE models; it is called an incubation parameter and is defined as

$$\gamma = \frac{V_{shear}}{V_{MPI}} \tag{27}$$

where all variables have their earlier meanings.

Independently, Tang (2010) found that the same parameter defines the point at which shear becomes lethal to a storm (he called γ a "ventilation index"). Tang and Emanuel (2010) showed that shear reduces the achievable potential intensity by diluting the thermodynamic efficiency of a TC with low entropy environmental air. The degree to which potential intensity is reduced is a function of the product of the shear and saturation deficit, which is the numerator of γ. The denominator normalizes the quantity across different climates. Hence low shear, low saturation deficits, and high potential intensities both minimize the thermodynamic effects of shear (Tang and Emanuel, 2010) and reduce the time required for cyclone genesis and intensification (Rappin et al., 2010). While the precise functional combination and weighting of individual these factors remain subject to further refinement, the theoretical foundation for their relevance in the genesis process has been made substantially stronger by recent work. We now examine how the incubation parameter varies in our simulations.

Figures 25 and 26 shows what happens to γ as the climate gets progressively warmer. In the tropics, especially in the boxed areas, the incubation parameter increases whereas in the subtropics, the incubation parameter decreases substantially. Thus, in warmer climates it will take relatively longer for TCs to organize and intensify in the tropics, and it will not take as long in the subtropics. In the tropics, MPI stays about constant, while shear decreases and χ increases. Thus, it appears that in the tropics, the

decrease in shear is not enough to overcome the increasing saturation deficit, meaning a relatively longer incubation time, or higher γ. Likewise, in the subtropics, χ increases, but shear decreases and MPI increases substantially. Thus, in spite of the growing saturation deficit, the incubation time for TC genesis and intensification decreases significantly mostly due to the large MPI increase.

Figure 27 shows the seasonal cycle for γ. Consequences of the unrealistically cold east Pacific in the UH0 case are seen here, with extraordinarily high values of γ occurring in the summer months. The general shape is to be expected, with lowest incubation times occurring in the summer months, and highest occurring in the late winter and early spring months. There is little change in the August-October values between the UH cases. However, the general trend is that as the climate warms, γ increases up until the UH3 case (3 doublings of CO_2, 2240 ppm), then begins to decrease again as you continue to warm into the UH4 and UH5 cases (4480 ppm, 8960 ppm, respectively). Since χ increases in a warming climate, in these two warmest scenarios, either MPI is increasing or shear decreasing (or both). Looking back at Figure 4 and Figure 20, the PD case and UH1, UH2, and UH3 cases, there is little change to wind shear or MPI within the boxes and the northern hemisphere as a whole. Thus, increasing saturation deficits swamp any change in the shear and MPI, resulting in an increased incubation time. For the UH4 and UH5 cases, there is a downward tick in wind shear, and a corresponding uptick in MPI. These combine to more than offset the increasing saturation deficits, resulting in decreased γ.

The joint distribution of γ and SST is shown in Figure 28. Note that within any particular climate, γ is fairly insensitive to SST—the distributions are more nearly vertical than tilted within the areas most prone to TC developments (particularly so in the Pacific; see panels c and d)—but as the entire climate warms from case to case, incubation times increase. The influence of globally rising temperatures on γ is complex: while warmer temperatures cause χ to rise, this is offset by declining shears and, in the case of the hottest climate, rising MPI. All together, as the climate warms the magnitude of the incubation parameter increases where it is lowest today, but it falls in many of the other parts of the tropics where it is high today. The end result is a broader area of generally low incubation values, though these are slightly larger than the lowest values found today. A recurring prediction from analysis of TC activity in models of anthropogenic warming has been that the number of cyclones will decline by the year 2100 as the climate warms (Knutson et al. 2007; Knutson et al. 2010); Emanuel et al. (2008) argued the rise in saturation deficits explains this trend, and here we see that the tempering effects of rising MPI and declining shears do not completely offset the upward pull that growing χ has on the incubation time for TC development.

5.2. Genesis potential index (GPI)

As described in Section 2, the GPI was created based on climactic factors described as important by Gray (1979), later enhanced by Emanuel and Nolan (2004), and further enhanced by Emanuel (2010). The empirical nature of these equations means that GPI is a best-fit curve to historical data points of TC cyclogenesis. In

differing climates, the components may not represent the areas of TC genesis well. However, the GPI equations should at least give us some ideas about how TC genesis will evolve over a warming climate. Hereafter, the first GPI equation (1) will be referred to as GPI_1, and the second GPI equation (2) will be referred to as GPI_2. Note that the units of GPI_1 do not make physical sense, and thus will be omitted.

Tippett et al. (2011) found that TC genesis is sensitive to the amount of vorticity where there are scant amounts of it, but that once some threshold value is passed, the other factors (thermodynamic and shear) become rate limiting. In both reanalysis data (Tippett et al. 2011) and high-resolution simulations at GFDL (S. Camargo, personal communication 2011), this threshold appears to be around an absolute vorticity of $4*10^{-5}$ s^{-1}, hereafter referred to as the absolute vorticity limit (AVL), which is roughly the value the Coriolis parameter achieves at 16° latitude. The argument is that equatorward of this point, TC development is highly dependent on the presence of elevated cyclonic (relative) vorticity, but poleward of it other factors are more important. While the genesis potential of a particular event may be higher in the presence of locally elevated vorticity from one day to the next, at least in the monthly mean an increase in the abundance of vorticity at higher latitudes does not appear to augment the ability of cyclones to form (Tippett et al. 2011).

Figures 29-32 show the spatial configuration of both GPI equations for the PD, PD3, and PD5 cases. Figures 29 and 31 are GPI_1 and GPI_2, respectively, both with no AVL, and Figures 30 and 32 are GPI_1 and GPI_2, respectively, both with AVL. The difference the AVL makes becomes quite apparent in both forms of the GPI, especially

in the west Pacific. Values in GPI_1 in the PD5 case fall from over 20, to around 8, and GPI_2 values fall from 15 to about 3 in the PD5 case. Thus, it is clear that instituting the AVL acts to lower genesis potential, due to the lower values of absolute vorticity poleward of 16°N latitude. Using the AVL GPI plots, some other trends can be seen. As a whole, GPI_1 and GPI_2 decrease in a warming climate, especially in the boxed regions. This decrease coincides with a slightly lower MPI and an increasing saturation deficit in these regions. However, in the subtropics, GPI increases substantially, due mainly to the large increase in MPI in these areas.

The seasonal cycles for GPI_1 and GPI_2 (with the AVL instituted) are shown in Figures 33 and 34, respectively. Note that the seasonal cycles of both GPI_1 and GPI_2 keep the same shape regardless of whether or not the AVL is used. The only difference comes in the amplitude of the respective GPI values. The lack of climate sensitivity, by ignoring the ever-growing saturation deficit, can be seen by comparing the two figures. As the climate warms, GPI_1 steadily increases, but GPI_2 decreases, due to the climate sensitivity that is not present in GPI_1, but is present in GPI_2, namely the saturation deficit. The use of RH instead of χ renders GPI_1 immune to the changes in climate (aside from changes to the individual variables associated with the changing climate), whereas χ is sensitive to the climate and accounts for the growing saturation deficit associated with a warming climate. Thus, on average, GPI_1 increases in a warming climate, and GPI_2 decreases.

6. SUMMARY AND CONCLUSIONS

We looked at nine scenarios that used the level of CO_2 to control the temperature of the atmosphere: 280 ppm (UH0), 355 ppm (PD), 560 ppm (UH1), 1120 ppm (UH2), 2240 ppm (UH3 and PD3), 4480 ppm (UH4), 8960 ppm (UH5 and PD5), where the PD cases include aerosol forcings, while the UH cases do not. OHT was fixed in all cases, which presented unrealistic cooling in the equatorial region of the east Pacific in UH0. Hence, the PD case was used as the control case for comparison. We then identified important factors of TC genesis and looked to see how they change in a progressively warmer climate. The four factors we considered were MPI, 200-850 mb vertical wind shear, mid-tropospheric moisture (both RH and χ, see discussion in Section 4b), and 850 mb absolute vorticity. We then looked to see how specific combinations and weightings of these factors changed in a warming climate, namely GPI_1 (Eqn. 1), GPI_2 (Eqn. 2), and γ (Eqn. 27). Both GPI formulas are best fit curves to historical TC genesis data, while γ, a ventilation index, is related to the required incubation time for a disturbance to form (see section 5 for discussion).

This study has shown that in a warming climate, the subtropics generally become more favorable for TC genesis and intensification, while the tropics generally becomes less favorable, especially in the regions where development is prevalent in today's climate. In the subtropics, reduced shear combined with large increases in the MPI overcome the increasing saturation deficit to increase the GPI and decrease the incubation time, γ, thereby becoming more favorable for TC genesis. Reduced MPI, due

to minimal increases in SST, combined with the increasing saturation deficit act to reduce GPI and increase γ, thereby decreasing TC favorability in the tropics. Overall, the general trend in the northern hemisphere is for a decrease in TC genesis. This decrease may be linked to changes in the hydrological cycle, manifested in a weakening of the Walker Circulation (Held and Soden, 2006; Vecchi and Soden, 2007a). Smaller-scale features act to either enhance activity in the subtropics or decrease activity in the tropics. For example, the poleward shift of convection caused by the poleward expansion of the Hadley cell in a warmer environment would cause more activity in the subtropics, while a decrease in low-latitude vorticity could hamper development of systems there.

What is currently unknown is how well these genesis indices represent actual TC genesis and behavior in different climates. For example, does the decrease in MPI and increase in saturation deficit in the tropical regions mean a significant change in TC genesis and intensification time? A next step would be to identify and track model-like TCs (possibly requiring a higher resolution model) so that changes to their numbers and strength can be followed across simulations. Such an effort, in combination with the results presented in this thesis, could be useful in refining GPI and calibrating it to a specific GCM.

REFERENCES

Abbot, D.S., M. Huber, G. Bousquet, and C. C. Walker, 2009: High-CO_2 cloud radiative forcing feedback over both land and ocean in a global climate model. *Geophysical Research Letters*, **36**, L05702, doi:10.1029/2008GL036703.

Barreiro, M.**,** A. Cherchi, and S. Masina, 2011: Climate sensitivity to changes in ocean heat transport. *Journal of Climate,* **in press***,* doi:10.1175/JCLI-D-10-05029.1.

Bister, M., and K. Emanuel, 1998: Dissipative heating and hurricane intensity. *Meteorology and Atmospheric Physics*, **65**, 233–240.

Bister, M., and K. A. Emanuel, 2002: Low frequency variability of tropical cyclone potential intensity: 1. Interannual to interdecadal variability. *Journal of Geophysical Research-Atmospheres*, **107**(D24): 4801, doi:10.1029/2001JD000776.

Bohren, C. F., and B. A. Albrecht, 1998: *Atmospheric Thermodynamics.* Oxford University Press, New York, NY, 402 pp.

Burpee, R. W., 1972: The origin and structure of easterly waves in the lower troposphere in north Africa. *Journal of the Atmospheric Sciences*, **29**, 77-90.

Caballero, R., and M. Huber, 2010: Spontaneous transition to super-rotation in warm climates simulated by CAM3. *Geophysical Research Letters*, **37**, L11701, doi:10.1029/2010GL043468.

Camargo, S. J., K. A. Emanuel, and A. H. Sobel, 2007: Use of a genesis potential index to diagnose ENSO effects on tropical cyclone genesis. *Journal of Climate*, **20**, 4819–4834.

Charney, J. G., and M. E. Stern, 1962: On the stability of internal baroclinic jets in a rotating atmosphere. *Journal of the Atmospheric Sciences*, **19**, 159-172.

DeMaria, M., 1996: The effect of vertical shear on tropical cyclone intensity change. *Journal of the Atmospheric Sciences*, **53**, 2076–2087.

Dunkerton, T. J., M. T. Montgomery, and Z. Wang, 2009: Tropical cyclogenesis in a tropical wave critical layer: Easterly waves. *Atmospheric Chemistry and Physics,* **9**, 5587–5646.

Emanuel, K. A., 1986: An air–sea interaction theory for tropical cyclones. Part I: Steady-state maintenance. *Journal of the Atmospheric Sciences*, **43**, 585–604.

Emanuel, K. A., 1988: The maximum intensity of hurricanes. *Journal of the Atmospheric Sciences*, **45**, 1143–1155.

Emanuel, K. A., 1989: The finite-amplitude nature of tropical cyclogenesis. *Journal of the Atmospheric Sciences*, **46**, 3431-3456.

Emanuel, K. A., 1991: The theory of hurricanes. *Annual Review of Fluid Mechanics*. **23**, 179-196.

Emanuel, K. A., 2000: A statistical analysis of hurricane intensity. *Monthly Weather Review*, **128**, 1139-1152.

Emanuel, K. A., 2003: Tropical cyclones. *Annual Review of Earth and Planetary Sciences*, **31**, 75-104.

Emanuel, K. A., 2005: Increasing destructiveness of tropical cyclones over the past 30 years. *Nature*, **436**, 686–688.

Emanuel, K. A., 2010: Tropical cyclone activity downscaled from NOAA– CIRES reanalysis, 1908–1958. *Journal of Advances In Modeling Earth Systems*, **2**, doi:10.3894/JAMES.2010.2.1.

Emanuel, K. A., C. DesAutels, C. Holloway, and R. Korty, 2004: Environmental control of tropical cyclone intensity. *Journal of the Atmospheric Sciences*, **61**, 843-858.

Emanuel, K. A., and D. Nolan, 2004: Tropical cyclone activity and global climate, *Proc. of the 26th Conference on Hurricanes and Tropical Meteorology*, Miami, FL, 5, May, 240–241.

Emanuel, K. A., R. Sundararjan, and J. Williams, 2008: Hurricanes and global warming: results from downscaling IPCC AR4 simulations. *American Meteorological Society*, **89**, 347-367.

Frank, W. M., and E. A. Ritchie, 2001: Effects of vertical wind shear on the intensity and structure of numerically simulated hurricanes. *Monthly Weather Review*, **129**, 2249–2269.

Frierson, D. M. W., J. Lu, and G. Chen, 2007: The width of the hadley circulation in simple and comprehensive general circulation models. *Geophysical Research Letters*, **34**, L18804, doi:10.1029/2007GL031115.

Gray, W. M., 1968: Global view of the origin of tropical disturbances and storms. *Monthly Weather Review*, **96**, 669–700.

Gray, W. M., 1979: Hurricanes: Their formation, structure and likely role in the tropical circulation. *Meteorology Over Tropical Oceans*, Shaw, D. B., ed., Royal Meteorological Society, Bracknell, UK. pp. 155-218.

Held, I. M., and B. J. Soden, 2006: Robust responses of the hydrological cycle to global warming. *Journal of Climate*, **19**, 5686–5699.

Holland, G. J., 1997: The maximum potential intensity of tropical cyclones. *Journal of the Atmospheric Sciences,* **54**, 2519–2541.

Holton, J. R., 2004: *An Introduction to Dynamic Meteorology*. Elsevier Academic Press, Burlington, MA, 535 pp.

Hu, Y. and Q. Fu, 2007: Observed poleward expansion of the Hadley circulation since 1979. *Atmospheric Chemistry and Physics*, **7**, 5229–5236, doi:10.5194/acp-7-5229-2007.

Knutson, T. R., J. McBride, J. C. L. Chan, K. A. Emanuel, G. J. Holland, C. W. Landsea, I. M. Held, J. P. Kossin, A. K. Srivastava, and M. Sugi, 2010: Tropical cyclones and climate change. *Nature Geoscience,* **3**, 157-163, doi:10.1038/ngeo779.

Knutson, T. R., J. J. Sirutis, S. T. Garner, I. M. Held, and R. E. Tuleya, 2007: Simulation of the recent multidecadal increase of Atlantic hurricane activity using an 18-km-grid regional model. *Bulletin of the American Meteorology Society*, **88**, 1549–1565, doi:10.1175/BAMS-88-10-1549.

Korty, R. L., and T. Schneider, 2008: The extent of Hadley circulations in dry atmospheres. *Geophysical Research Letters,* **35**, L23803, doi:10.1029/2008GL035847.

Kossin, J. P., 2008: Is the North Atlantic hurricane season getting longer? *Geophysical Research Letters*, **35**, L23705, doi:10.1029/2008GL036012.

Landsea, C. W., B. A. Harper, K. Hoarau, and J. A. Knaff, 2006: Can we detect trends in extreme tropical cyclones? *Science*, **313**, 452–454.

Lu, J., G. A. Vecchi, and T. Reichler, 2007, Expansion of the Hadley cell under global warming. *Geophysical Research Letters*, **34**, L06805, doi:10.1029/2006GL028443.

Nolan, D. S., 2011: Evaluating environmental favorability for tropical cyclone

development with the method of point downscaling. *Journal of Advances in Modeling Earth Systems,* **in press**.

Nolan, D. S. and E. D. Rappin, 2008: Increased sensitivity of tropical cyclogenesis to wind shear in higher SST environments. *Geophysical Research Letters*, **35** *,* L14805, doi:10.1029/2008GL034147.

Nolan, D. S., E. D. Rappin, and K. A. Emanuel, 2007: Tropical cyclogenesis sensitivity to environmental parameters in radiative-convective equilibrium. *Quarterly Journal of the Royal Meteorological Society,* **133***,* 2085-2107.

Palmen, E., 1948: On the formation and structure of tropical hurricanes. *Geophysica*, **3**, 26-38.

Powell, M. D., S. H. Houston, L. R. Amat, and N. Morisseau-Leroy, 1998: The HRD real-time hurricane wind analysis system. *Journal of Wind Engineering and Industrial Aerodynamics*, **77**, 53–64.

Rappin, E. D., D. S. Nolan, and K. A. Emanuel, 2010: Thermodynamic control of tropical cyclogenesis in environments of radiative-convective equilibrium with shear. *Quarterly Journal of the Royal Meteorological Society*, **136**, 1954-1971.

Ruti, P.M. and A. Dell'Aquila, 2010: The twentieth century African easterly waves in reanalysis systems and IPCC simulations, from intra-seasonal to inter-annual variability. *Climate Dynamics*, **35**, 1099-1117, doi:10.1007/s00382-010-0894-z.

Seager, R., M. Ting, I. Held, Y. Kushnir, J. Lu, G. Vecchi, H.-P. Huang, N. Harnik, A. Leetmaa, N.-C. Lau, C. Li, J. Velez, and N. Naik, 2007: Model projections of an imminent transition to a more arid climate in southwestern North America. *Science*, **316**, 1181-1184.

Seidel, D. J., Q. Fu, W. J. Randel, and T. J. Reichler, TJ, 2008: Widening of the tropical belt in a changing climate. *Nature Geoscience*, **1**, 21–24.

Seidel, D. J. and W. J. Randel, 2007: Recent widening of the tropical belt: evidence from tropopause observations. *Journal of Geophysical Research*, **112**, D20113, doi:10.1029/2007JD008861.

Sherwood, S. and M. Huber, 2010: An adaptability limit to climate change due to heat stress. *Proceedings of the National Academy of Sciences*, www.pnas.org/cgi/doi/10.1073/pnas.0913352107.

Speelman, E. N., J. O. Sewall, D. Noone, M. Huber, A. von der Heydt, J. S. Damste, and G.-J. Reichart, 2010: Modeling the influence of a reduced equator-to-pole sea

surface temperature gradient on the distribution of water isotopes in the Early/Middle Eocene. *Earth and Planetary Science Letters*, **298**, 57–65.

Tang, B., 2010: Midlevel ventilation's constraint on tropical cyclone intensity. Ph.D. Thesis, Massachusetts Institute of Technology, Cambridge, MA.

Tang, B., and K. A. Emanuel, 2010: Mid-level ventilation's constraint on tropical cyclone intensity. *Journal of the Atmospheric Sciences,* **67**, 1817–1830.

Tippett, M. K., S. J. Camargo, and A. H. Sobel, 2011: A Poisson regression index for tropical cyclone genesis and the role of large-scale vorticity in genesis. *Journal of Climate*, **24**, 2335-2357.

Vecchi, G. A., and B. J. Soden, 2007a: Global warming and the weakening of the tropical circulation. *Journal of Climate*, **20**, 4316-4340.

Vecchi, G. A., and B. J. Soden, 2007b: Effect of remote sea surface temperature change on tropical cyclone potential intensity. *Nature*, **450**, 1066–1070.

Wallace, J. M., and P. V. Hobbs, 2006: *Atmospheric Science: An Introductory Survey.* Elsevier, Burlington, MA, 504 pp.

Webster, P. J., G. J. Holland, J. A. Curry, and H.-R. Chang, 2005: Changes in tropical cyclone number, duration, and intensity in a warming environment. *Science*, **309**, 1844–1846.

Williams, I., R. Pierrehumbert, and M. Huber, 2009: Global warming, convective threshold and false thermostats. *Geophysical Research Letters*, **36**, L21805, doi:10.1029/2009GL039849.

APPENDIX A

TABLES

Table 1: Overview of experiments.

Case	CO_2 level	Global SST	Tropical SST	No. yrs.
UH 0	280 ppm	15.2°C	22.8°C	20
UH 1	560 ppm	18.5°C	26.7°C	31
UH 2	1120 ppm	20.7°C	28.6°C	19
UH 3	2240 ppm	23.3°C	30.8°C	21
UH 4	4480 ppm	26.9°C	33.9°C	24
UH 5	8960 ppm	33.4°C	39.6°C	15
PD	355 ppm	16.3°C	25.6°C	25
PD 3	2240 ppm	23.0°C	30.7°C	19
PD 5	8960 ppm	34.0°C	40.1°C	19

We examined 9 cases in two distinct series in this study. Both the annual and global mean SST and annual and tropical mean SST are presented for each case. The number of years of available equilibrium output over which averages were computed is shown in the last column. UH stands for "ultra-hot", has a solar constant of 1365 W/m^2, and contains no aerosol forcings. PD stands for "present-day" (based on the 1990 CO_2 level of 355 ppm), has a solar constant of 1367 W/m^2, and contains aerosol forcings.

APPENDIX B

FIGURES

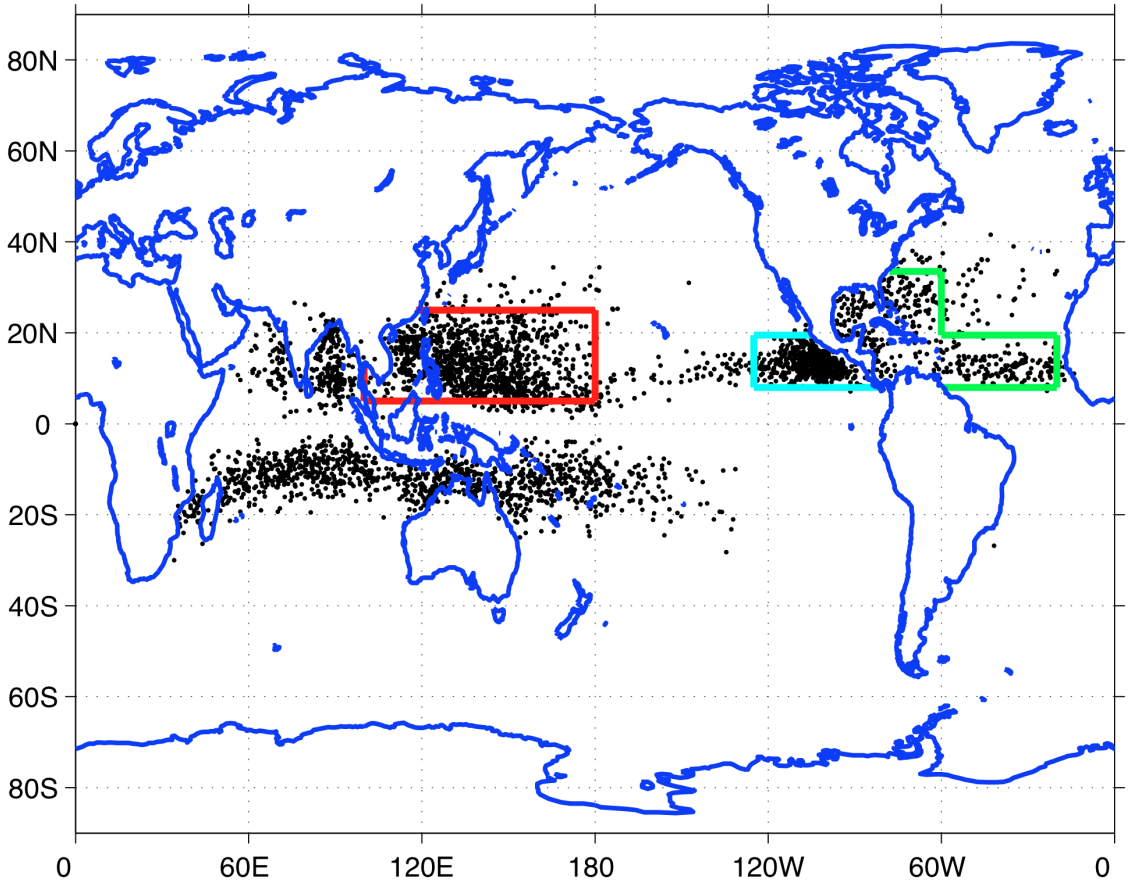

Figure 1: Tropical cyclone genesis locations between 1970 and 2008. Locations taken from HURDAT best track dataset. The boundaries used in subsequent analysis of the Western Pacific region are shown in red, boundaries for the Eastern Pacific are in cyan, and boundaries for the Atlantic are in green.

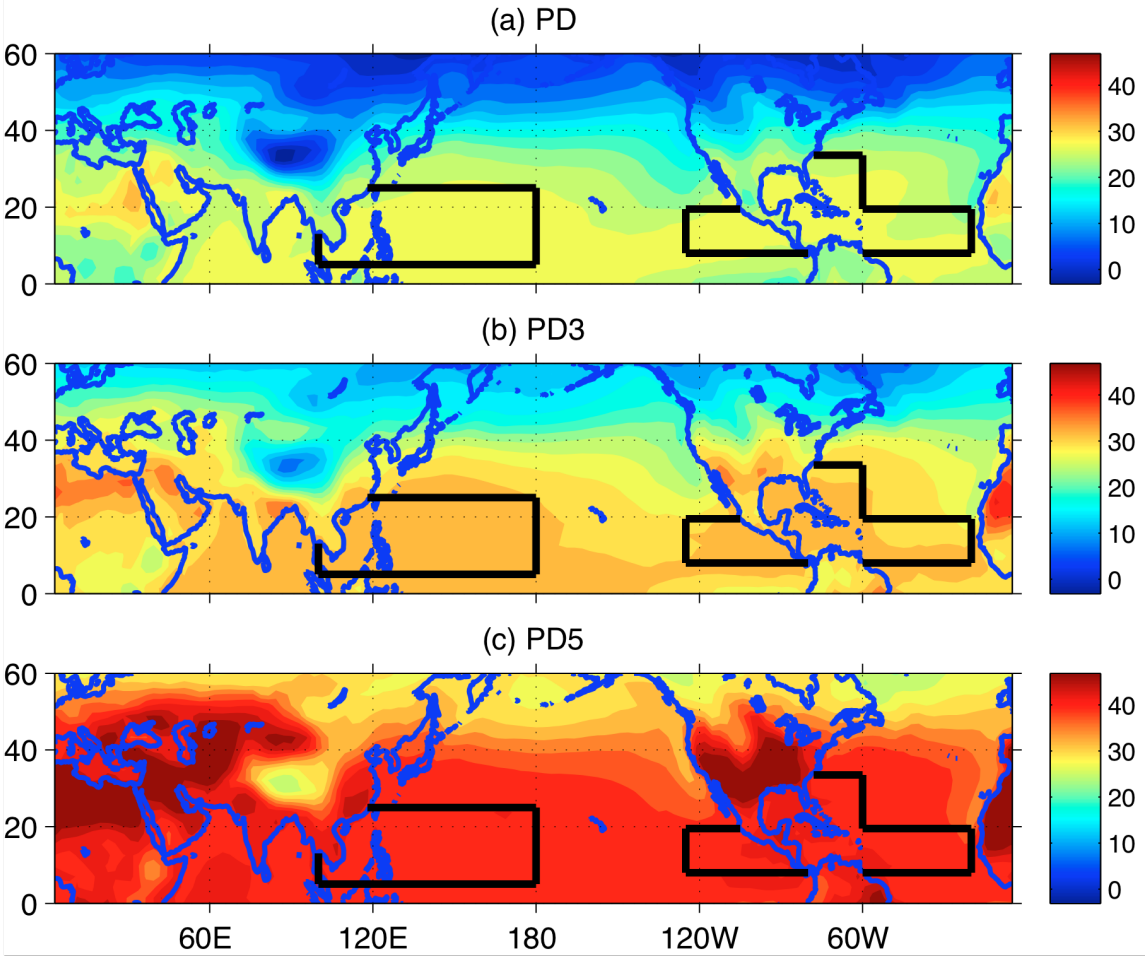

Figure 2: Annually averaged surface temperatures (SSTs) for PD cases. SSTs for (a) the PD case with 1990 levels of CO_2, (b) PD3 with 2240 ppm CO_2, and (c) PD5 with 8960 ppm CO_2. Contour intervals are 2.5°C.

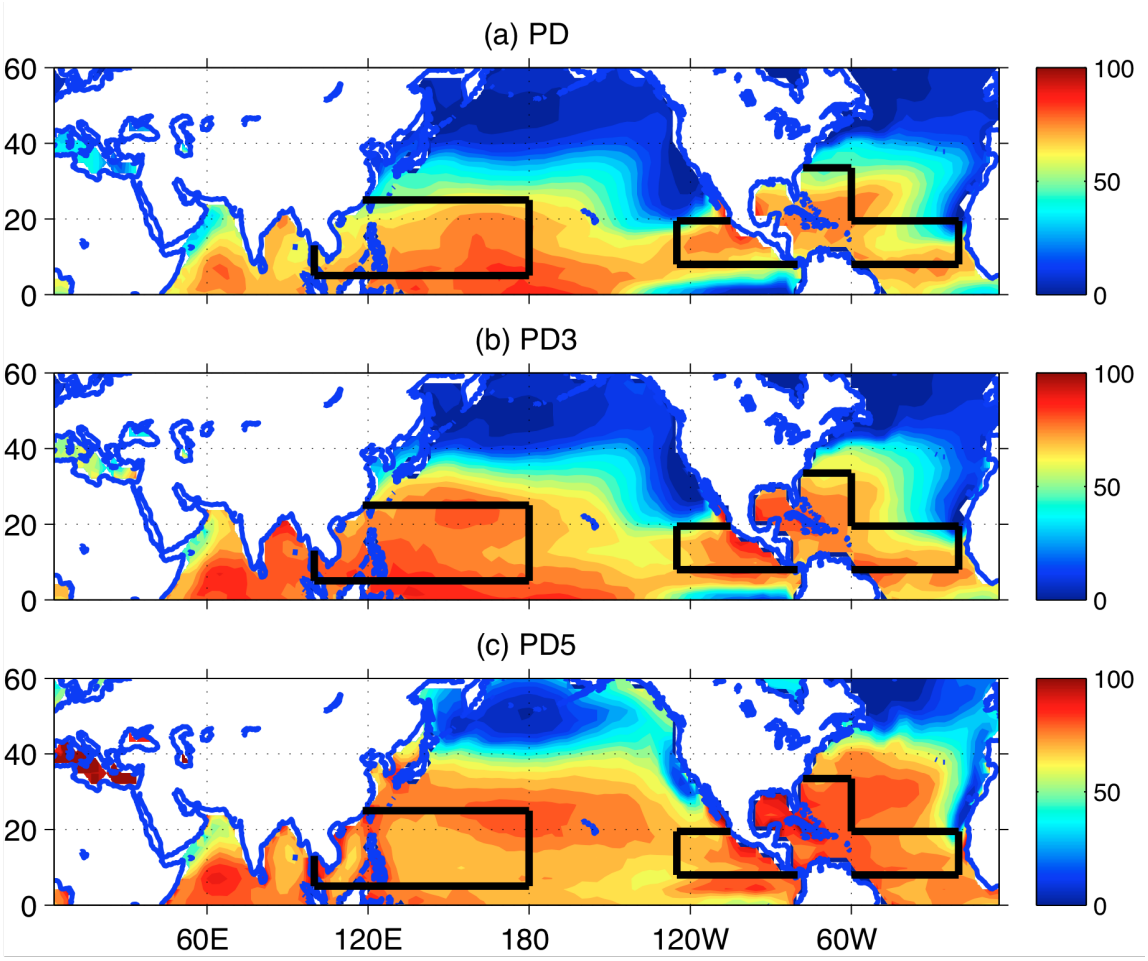

Figure 3: Maximum potential intensity (MPI) for PD cases. MPI averaged over all Augusts, Septembers, and Octobers for (a) PD, (b) PD3, and (c) PD5. Units are in m/s.

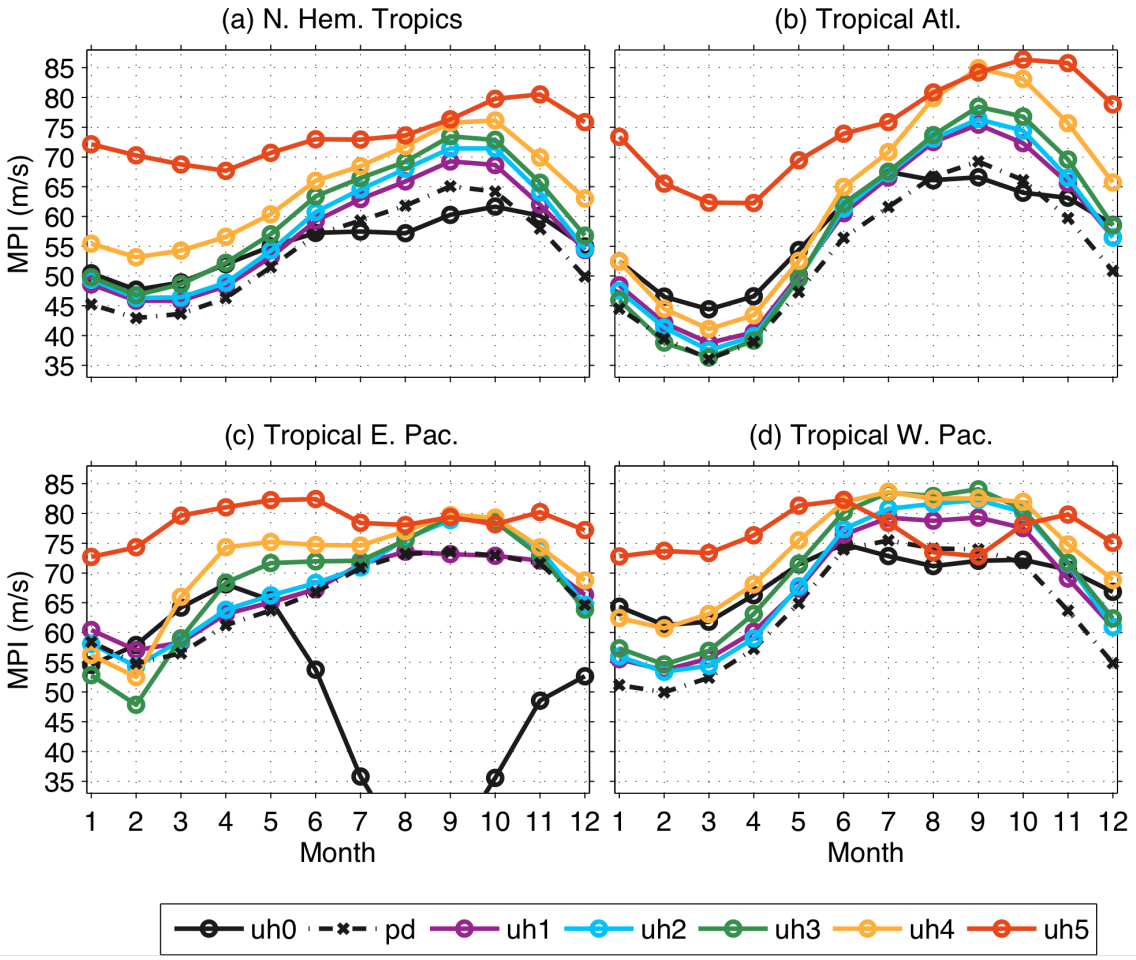

Figure 4: Annual cycle of MPI. MPI averaged over (a) the Northern Hemisphere tropics, (b) Atlantic box, (c) Eastern Pacific box, and (d) Western Pacific box. Refer to Figure 1 and text for definition of areas.

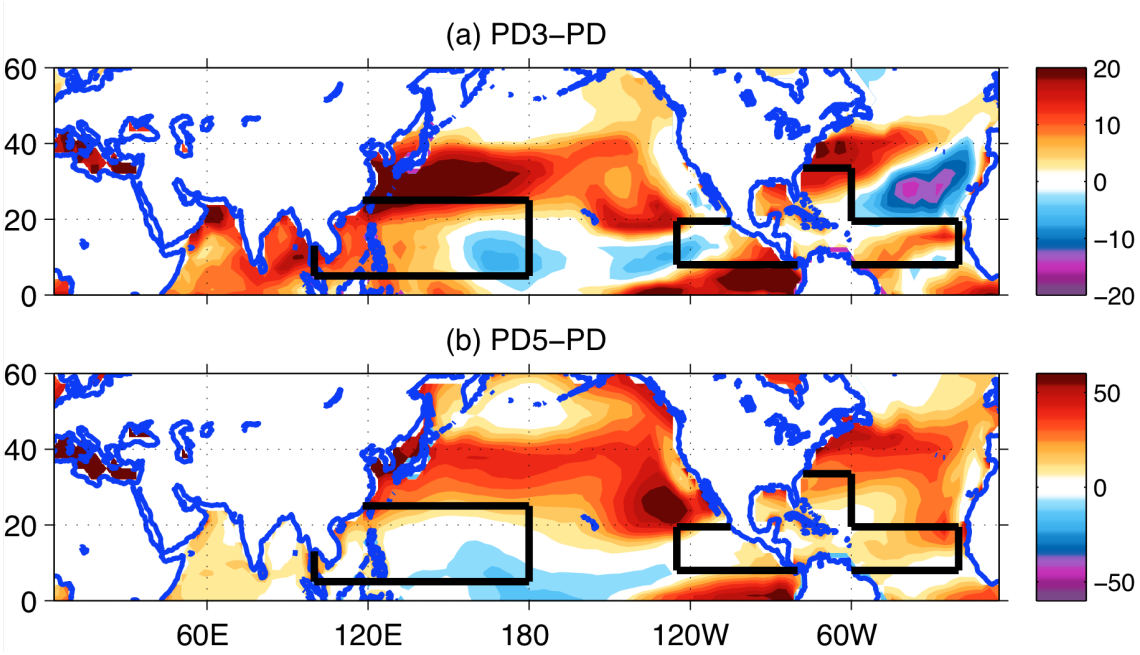

Figure 5: Change in August-October MPI. ΔMPI (m/s) between (a) PD3 and PD and (b) PD5 and PD. Contour interval is 2 m/s in panel (a) and 6 m/s in panel (b); note each panel uses a distinct colorscale.

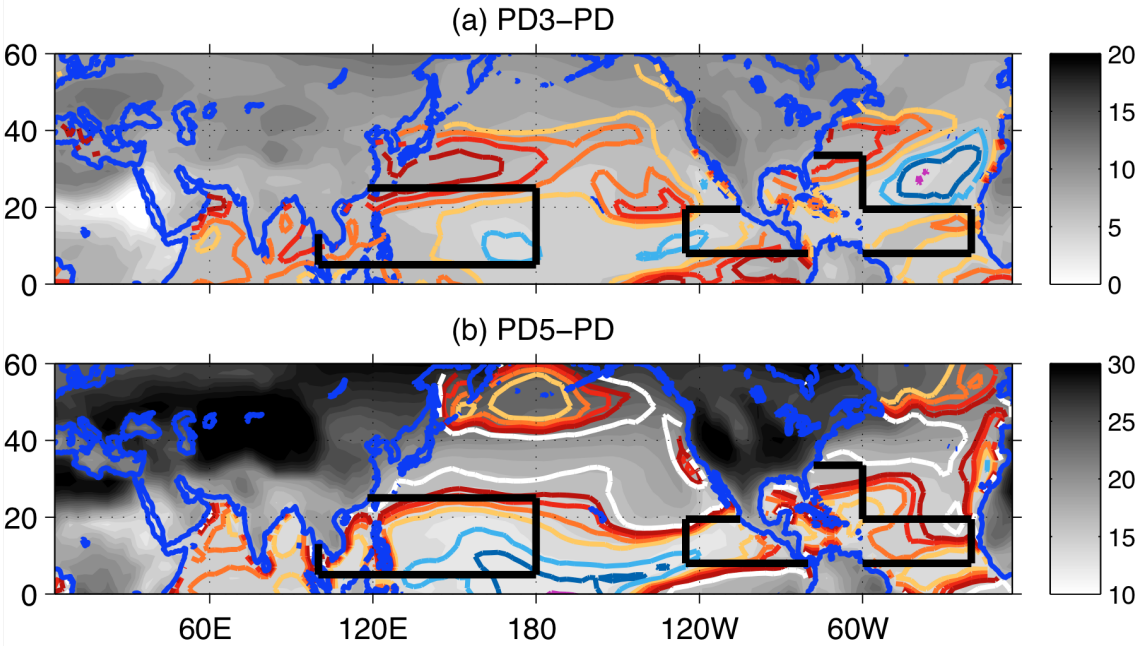

Figure 6: Change in August-October surface temperatures and MPI. Change in surface temperature (gray shading) and MPI (colored contours) between (a) PD3 and PD and (b) PD5 and PD. Note the gray colorscale covers different ranges in each panel. Values of MPI that decrease are shown in blues and purples in 5 m/s increments and values of MPI that increase are shown in oranges and reds in 5 m/s increments up to +20 m/s. The white contour indicates a change of +35 m/s.

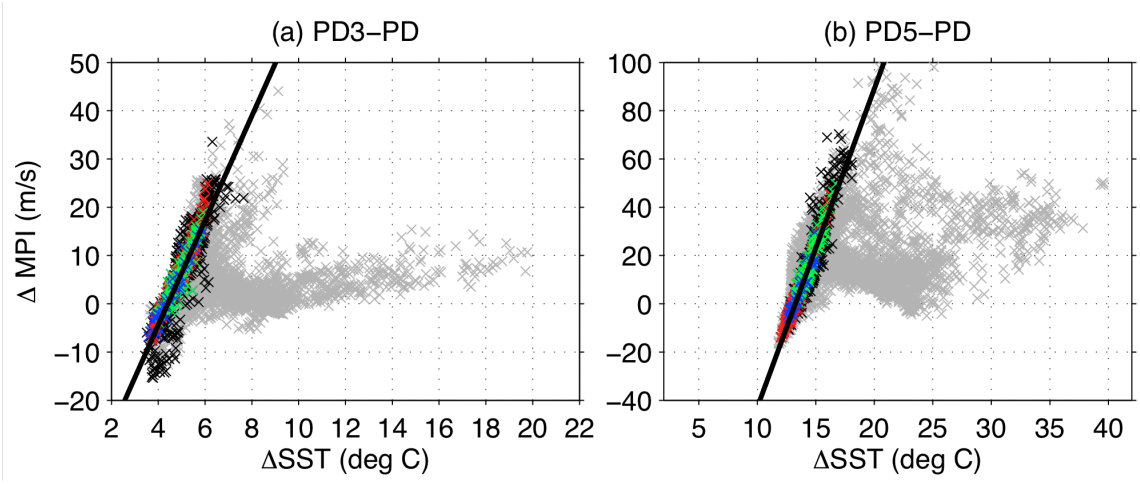

Figure 7: Scatter plot of difference in SST versus difference in MPI. Changes plotted between (a) PD3-PD and (b) PD5-PD. All points from the globe are shown in gray; those from the Northern Hemisphere tropics are black; those from the Western Pacific are red; those from the Eastern Pacific are blue; and those from the tropical Atlantic are green. The best-fit line through all Northern Hemisphere tropical points is shown; the correlation coefficient is 0.91 for (a) and 0.94 for (b).

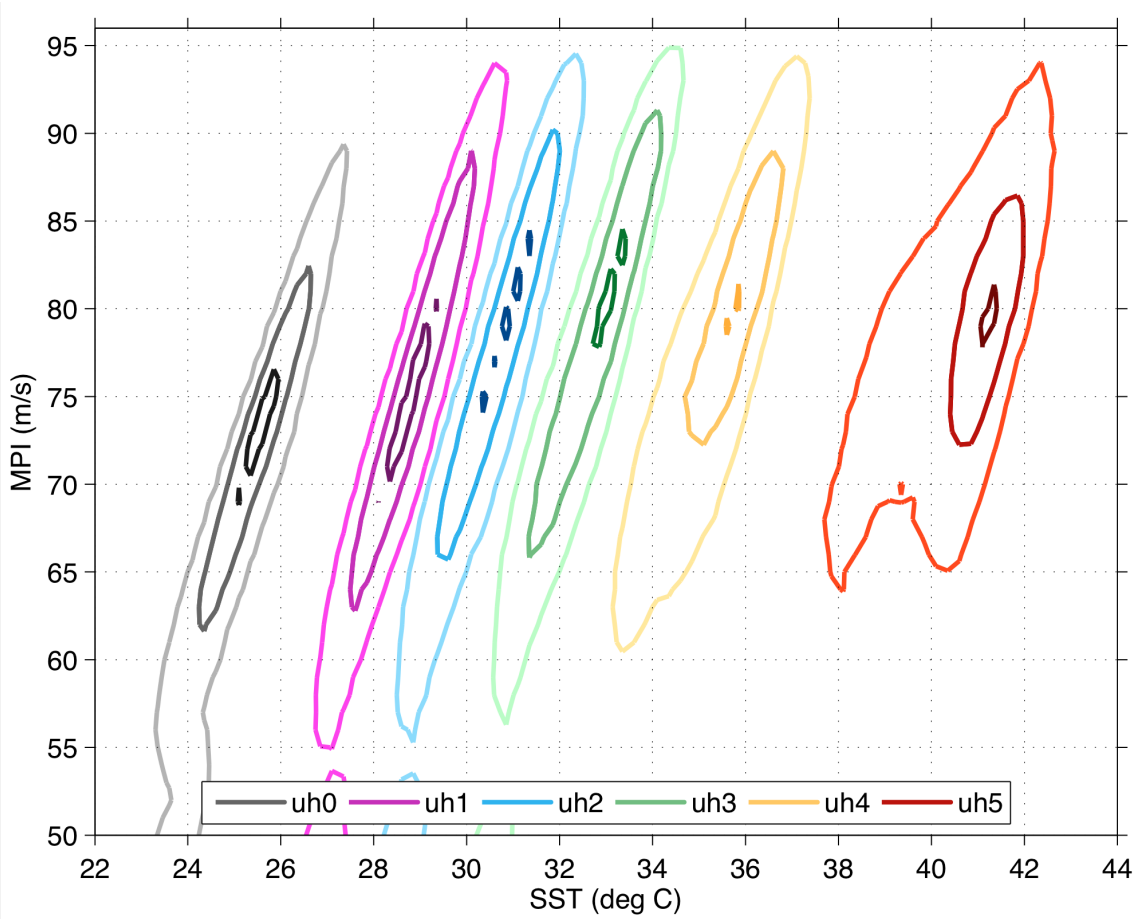

Figure 8: Joint distribution of SST and MPI. SST (˚C) and MPI (m/s) shown for UH cases. Darker contours indicate higher densities.

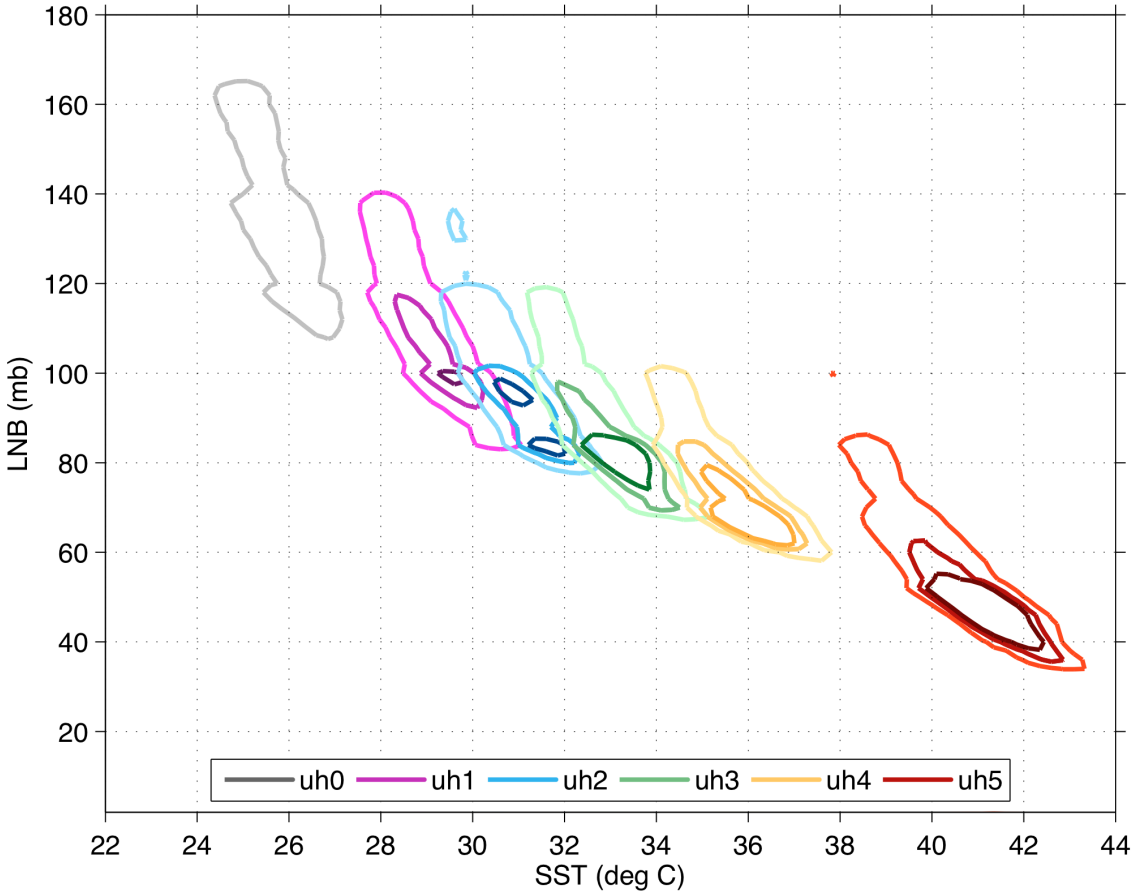

Figure 9: Joint distribution of SST and level of neutral buoyancy (LNB). LNB (mb) is the equilibrium level to which a parcel lifted from the sea surface rises.

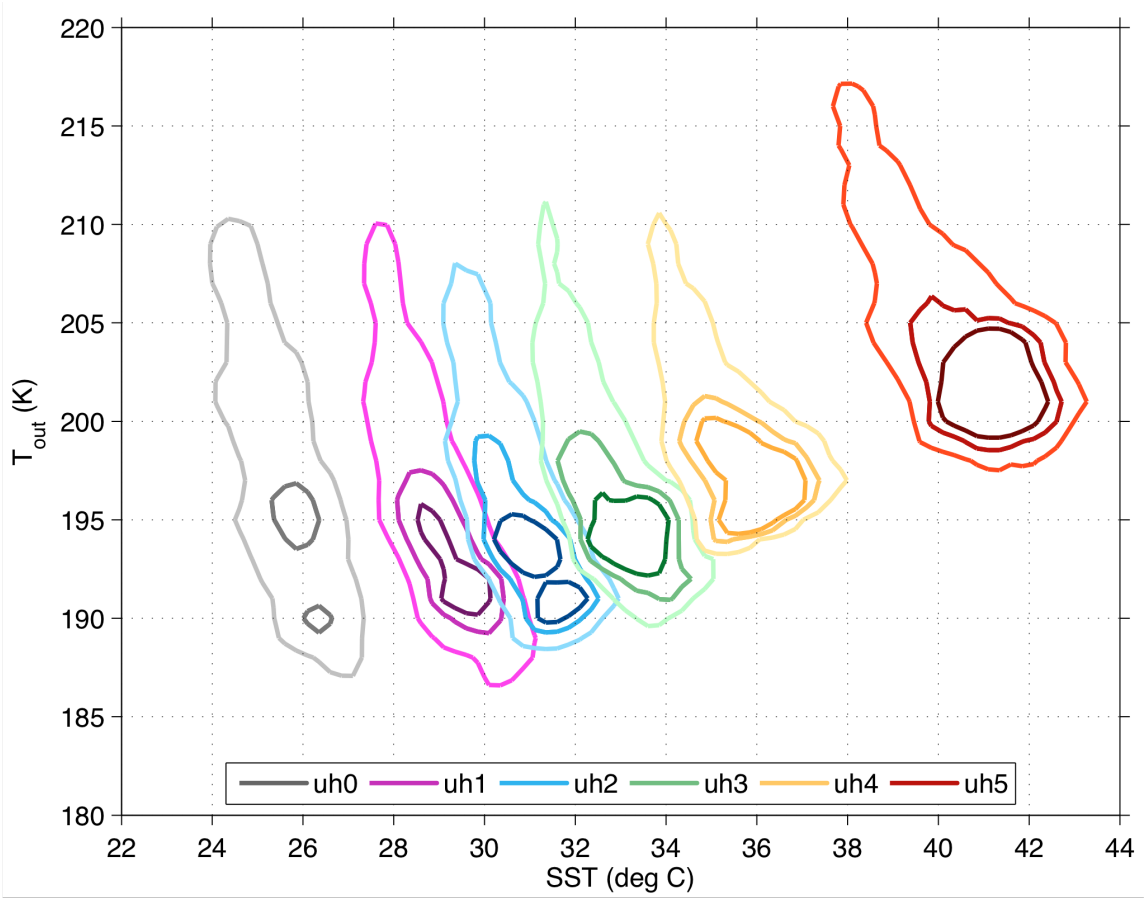

Figure 10: Joint distribution of SST and outflow temperature. Outflow temperature (K) is the temperature at the level of neutral buoyancy, which is the top of the positive area of convective available potential energy (CAPE) on a thermodynamic sounding.

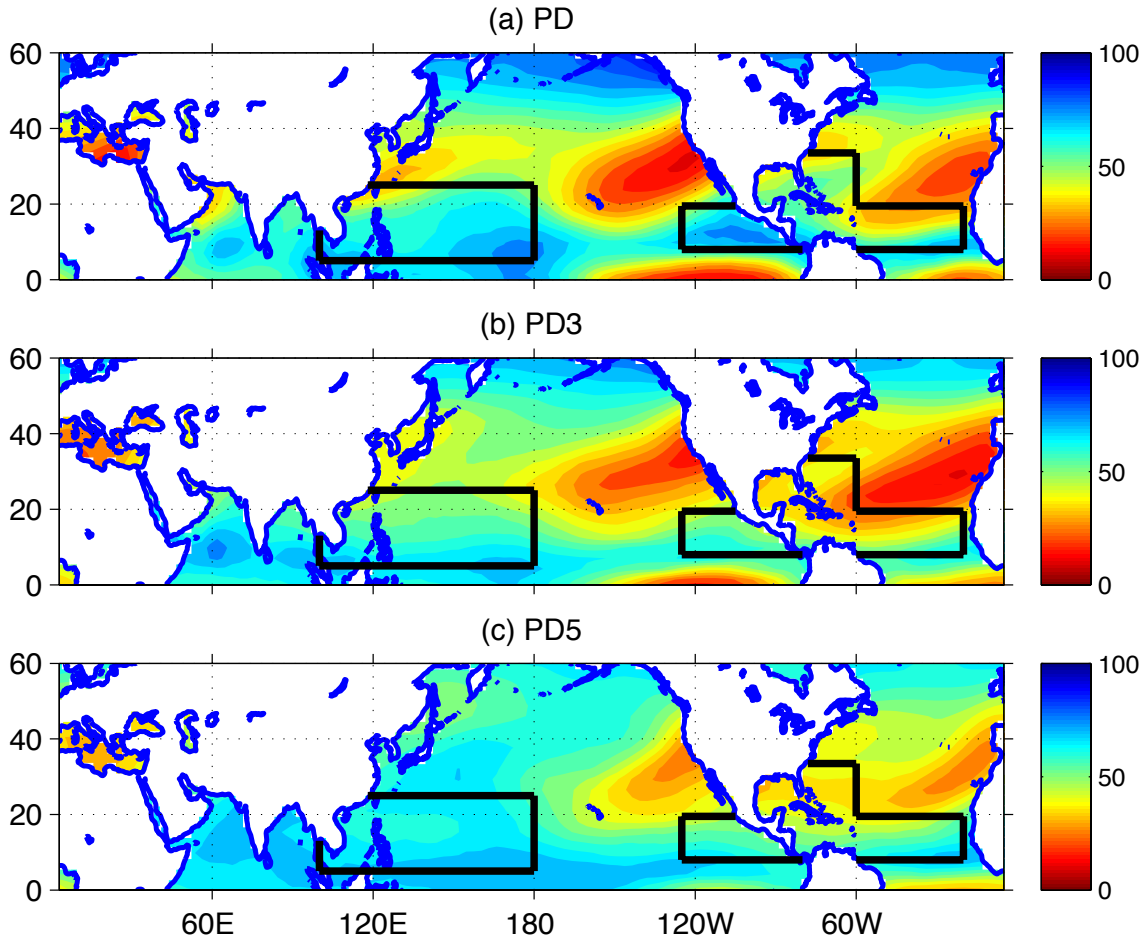

Figure 11: Relative Humidity (RH) in PD cases. RH averaged over all Augusts, Septembers, and Octobers for (a) PD, (b) PD3, and (c) PD5 cases. Note colorscale is inverted so that blue indicates high levels (moist) and red indicates dry conditions. RH given as %.

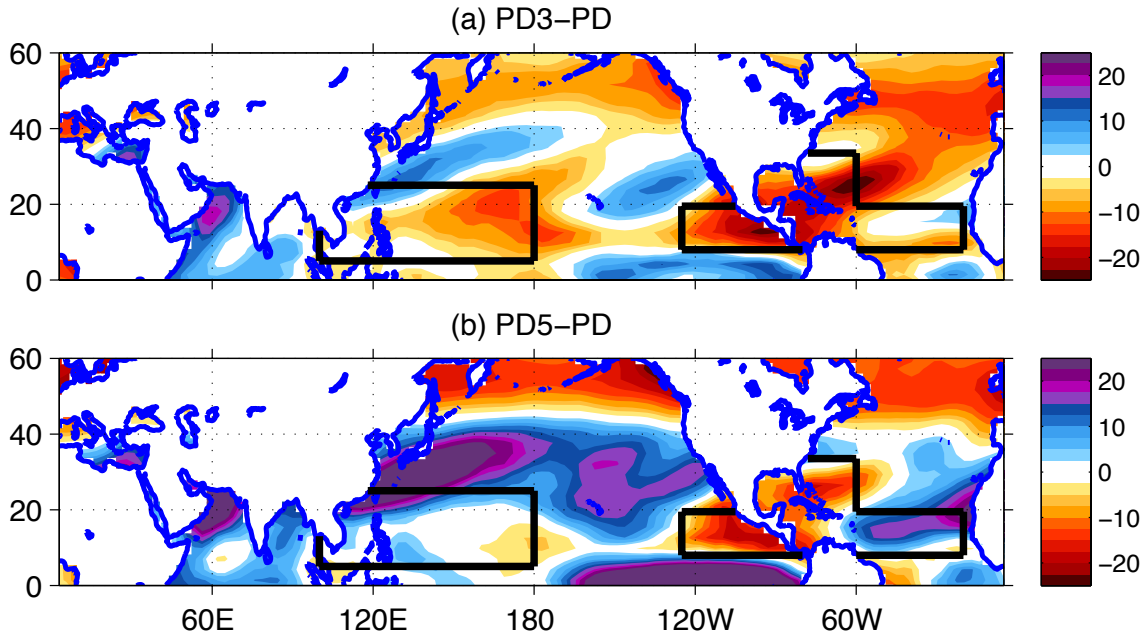

Figure 12: Change in August-October RH. ΔRH (%) between (a) PD3 and PD and (b) PD5 and PD.

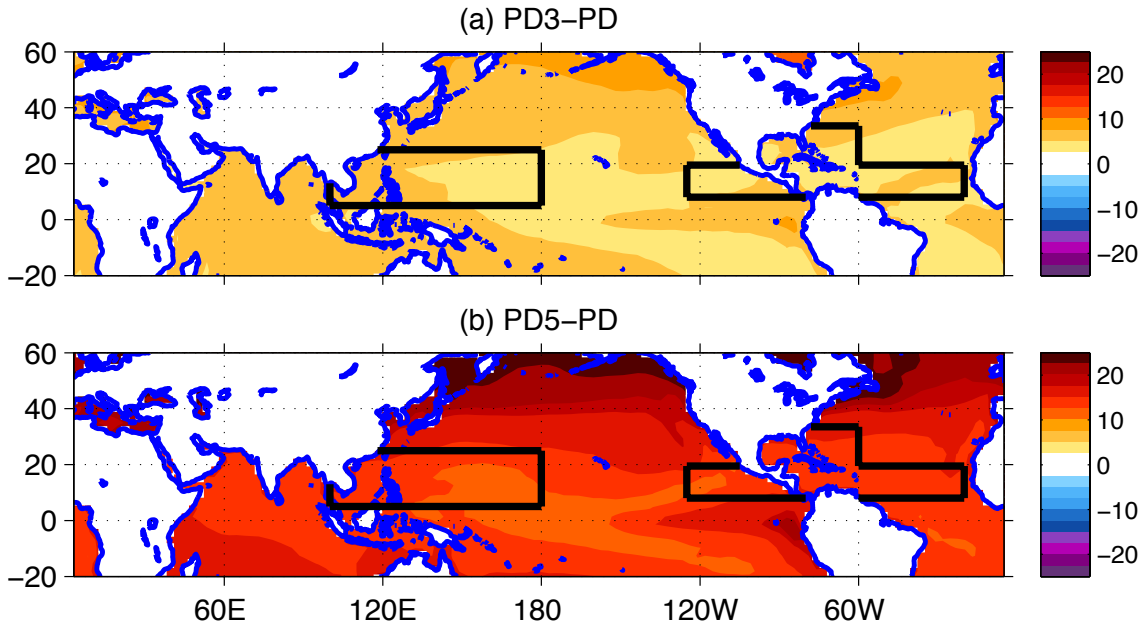

Figure 13: Change in peak season surface temperatures. August-October change in surface temperature between (a) PD3 and PD and (b) PD5 and PD.

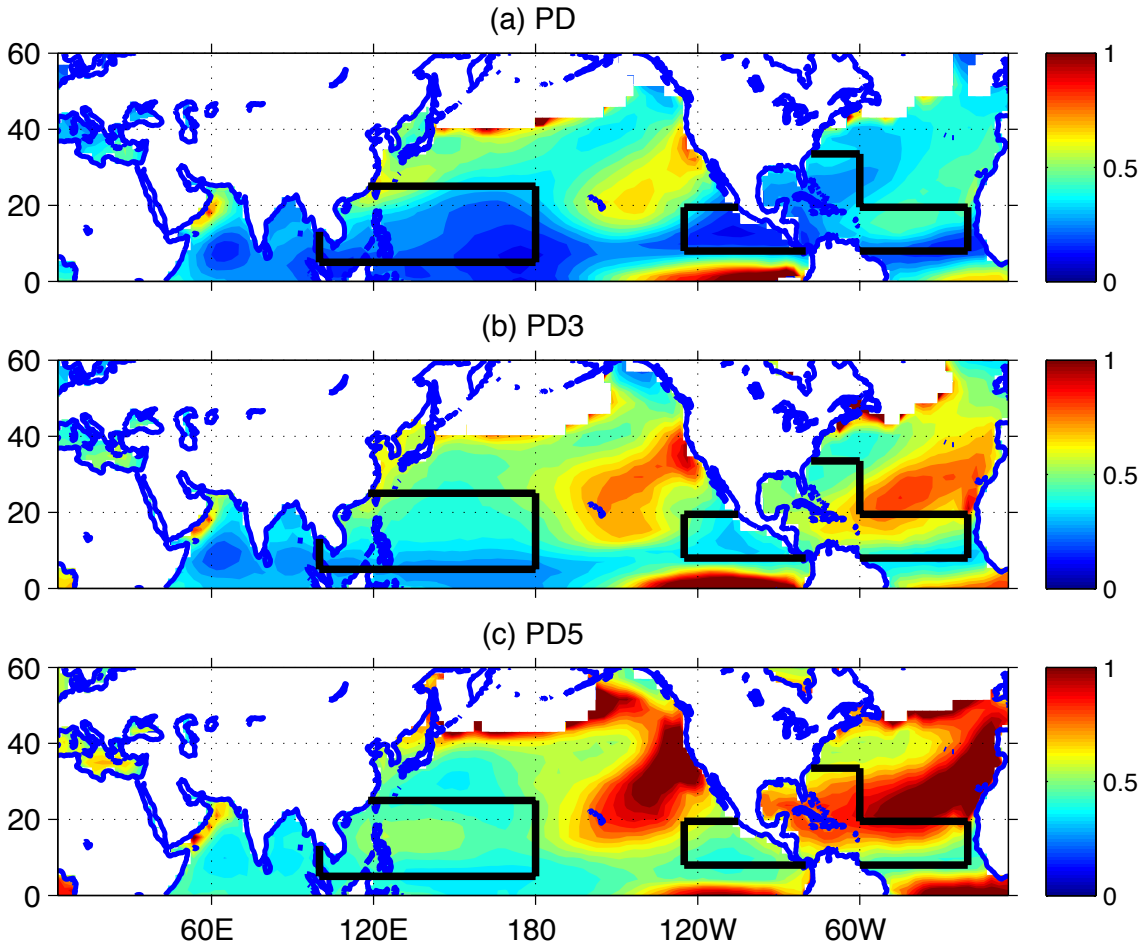

Figure 14: Non-dimensional entropy parameter χ in PD cases. χ averaged over all Augusts, Septembers, and Octobers for (a) PD, (b) PD3, and (c) PD5 cases.

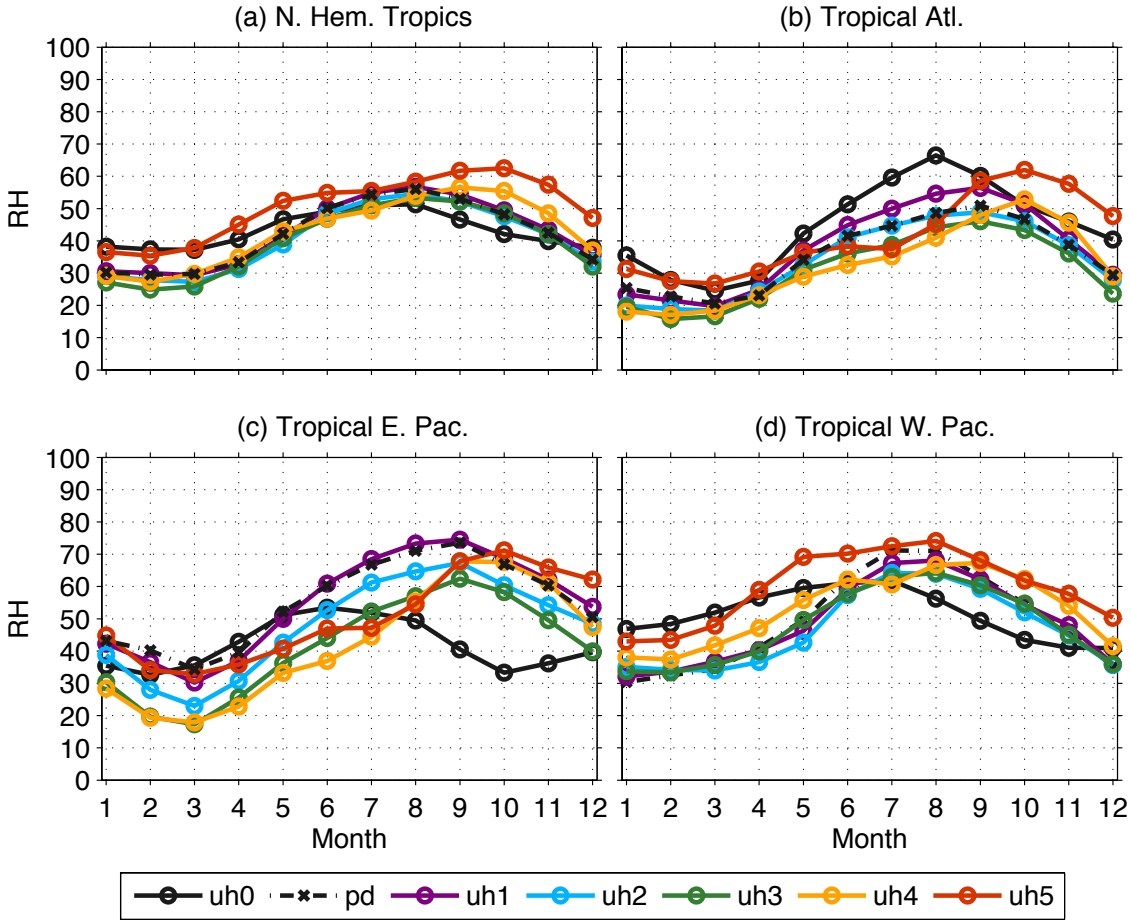

Figure 15: Annual cycle of Relative Humidity (RH). RH averaged over (a) the Northern Hemisphere tropics, (b) Atlantic box, (c) Eastern Pacific box, and (d) Western Pacific box. Refer to Figure 1 and text for definition of areas.

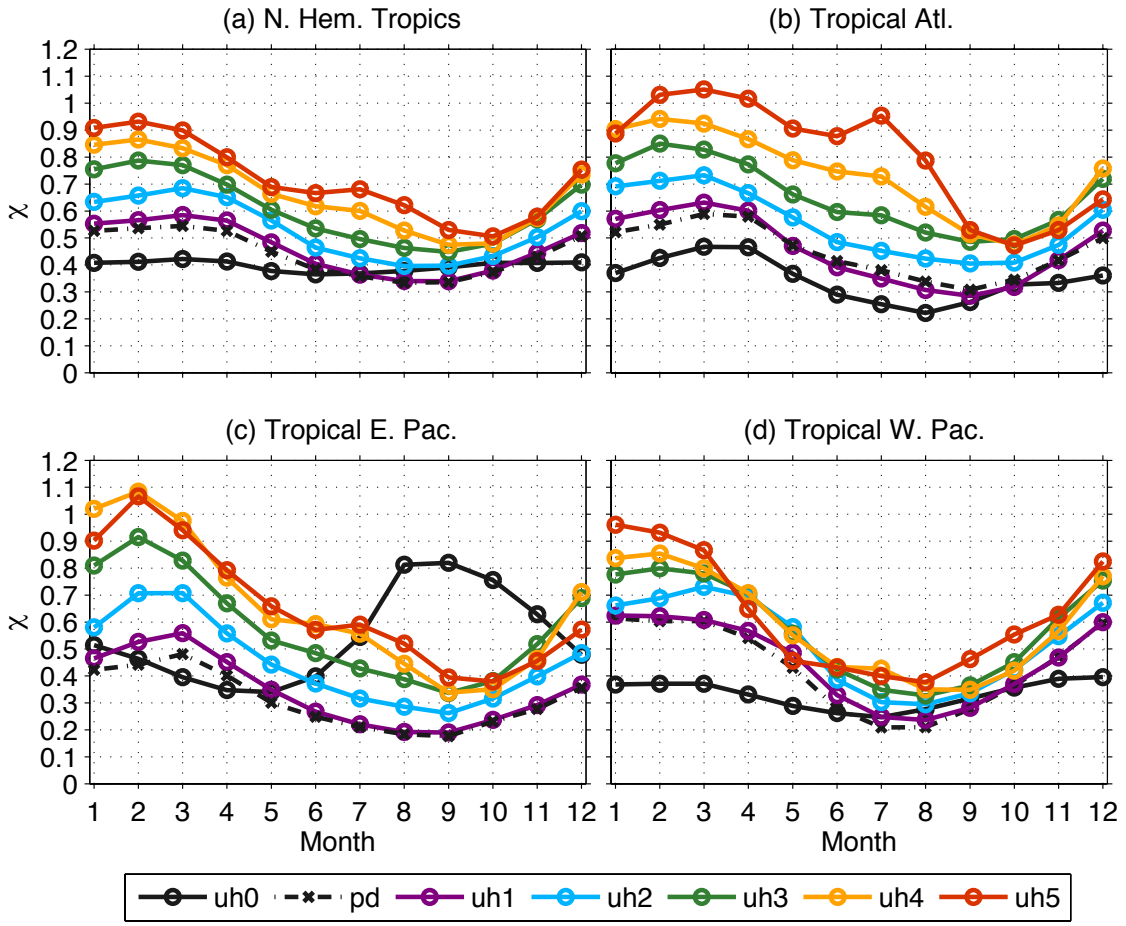

Figure 16: Annual cycle of χ. χ averaged over (a) the Northern Hemisphere tropics, (b) Atlantic box, (c) Eastern Pacific box, and (d) Western Pacific box. Refer to Figure 1 and text for definition of areas.

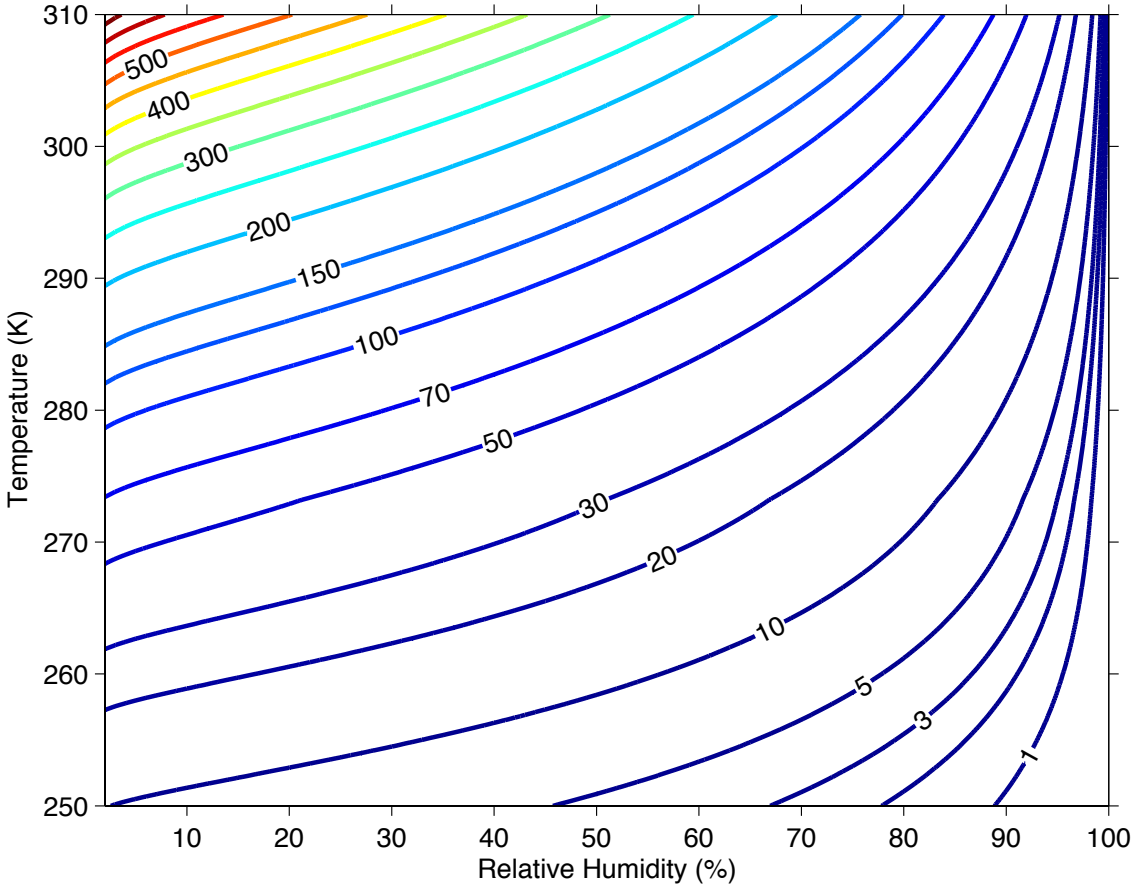

Figure 17: Saturation entropy deficit as a function of RH and T. RH (x-axis) given in %, T (y-axis) given in K, saturation entropy deficit (s* - s) given as units of J kg^{-1} K^{-1}.

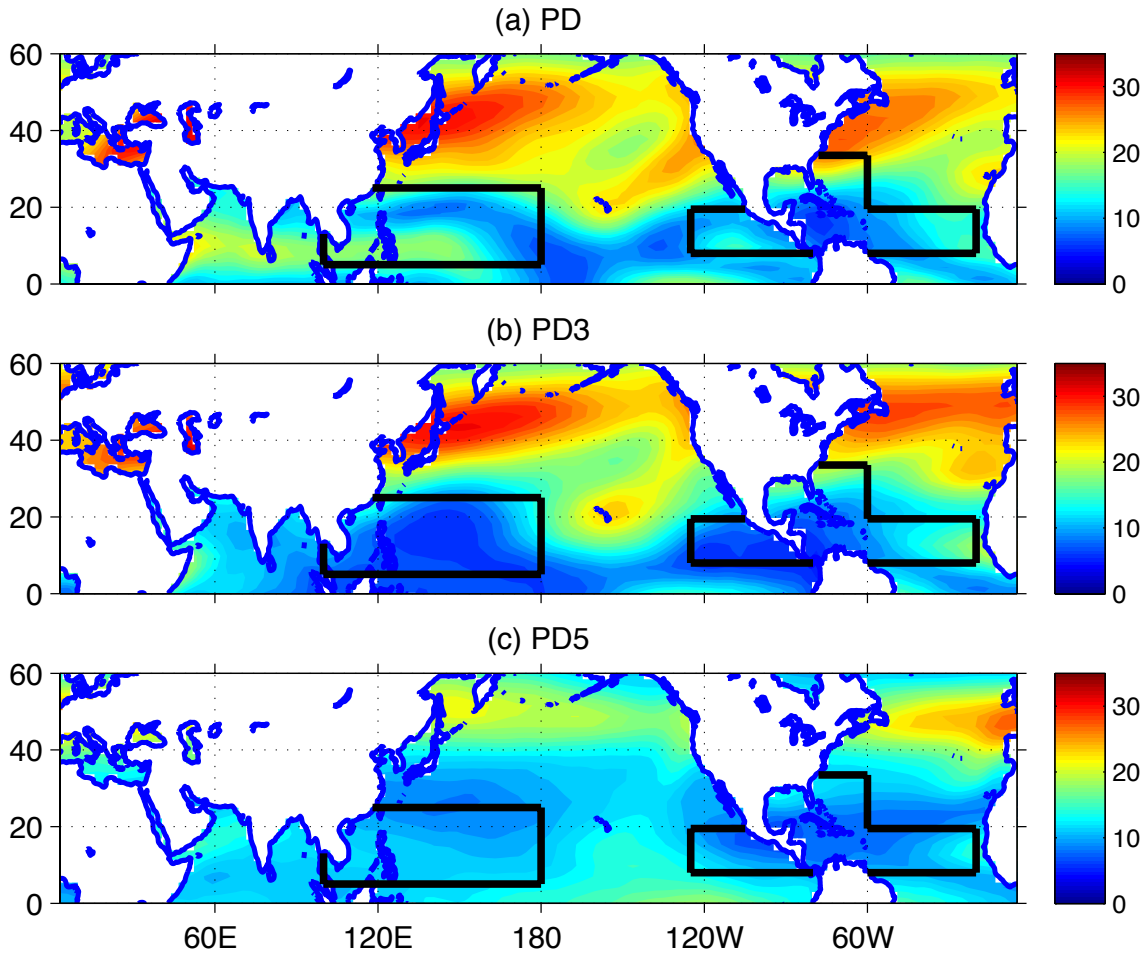

Figure 18: Wind shear in PD cases. Shear (m/s) averaged over all Augusts, Septembers, and Octobers for (a) PD, (b) PD3, and (c) PD5 cases.

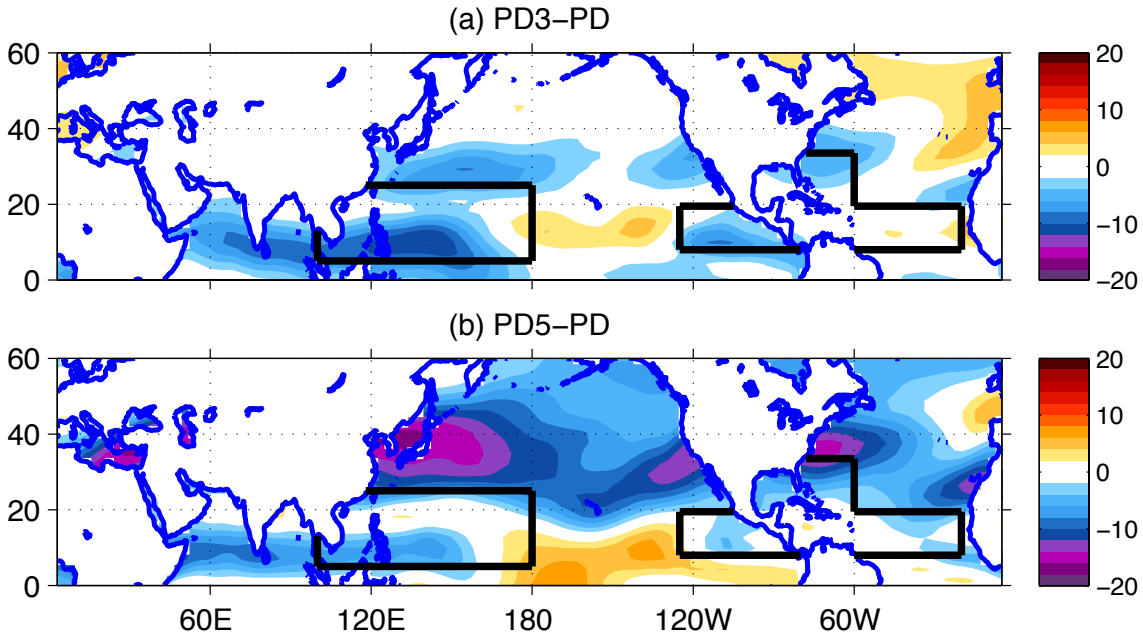

Figure 19: Change in August-October wind shear. Change in wind shear (m/s) between (a) PD3 and PD and (b) PD5 and PD.

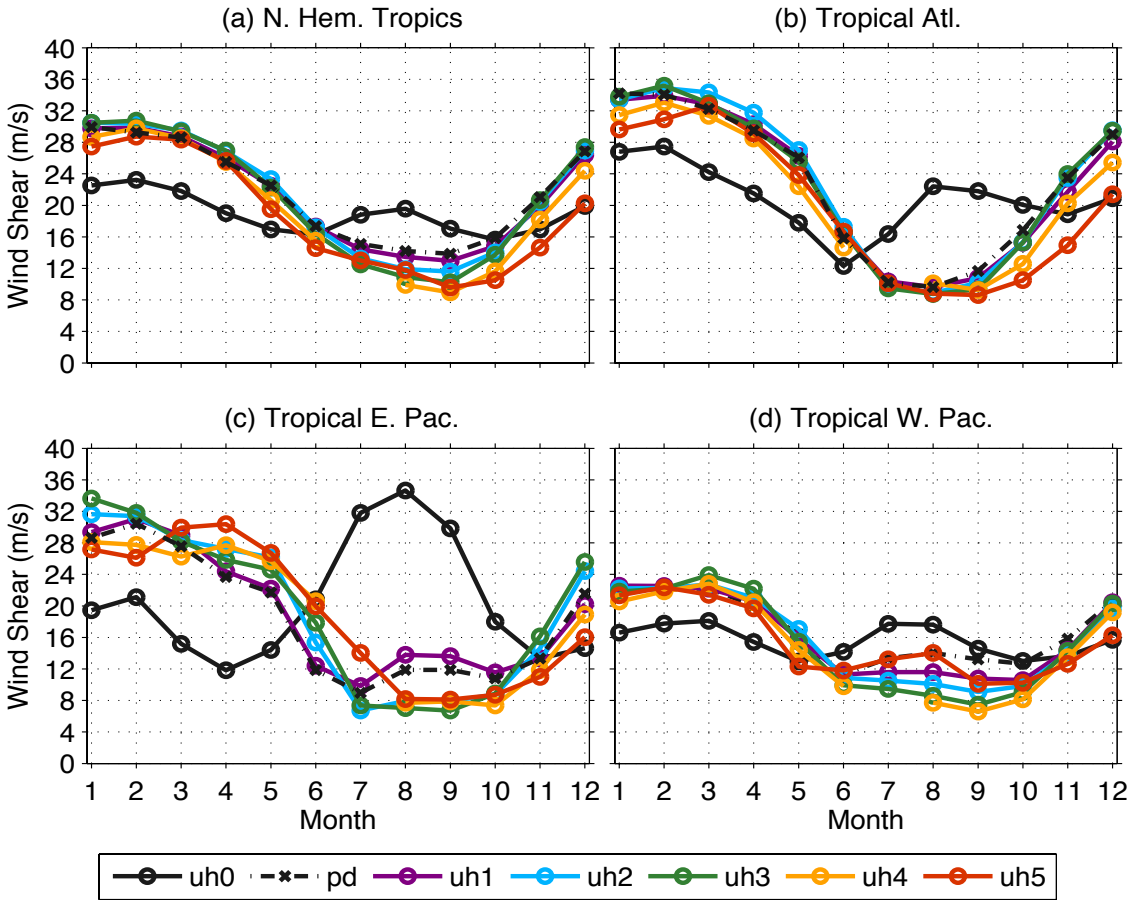

Figure 20: Annual cycle of wind shear. Wind shear averaged over (a) the Northern Hemisphere tropics, (b) Atlantic box, (c) Eastern Pacific box, and (d) Western Pacific box. Refer to Figure 1 and text for definition of areas.

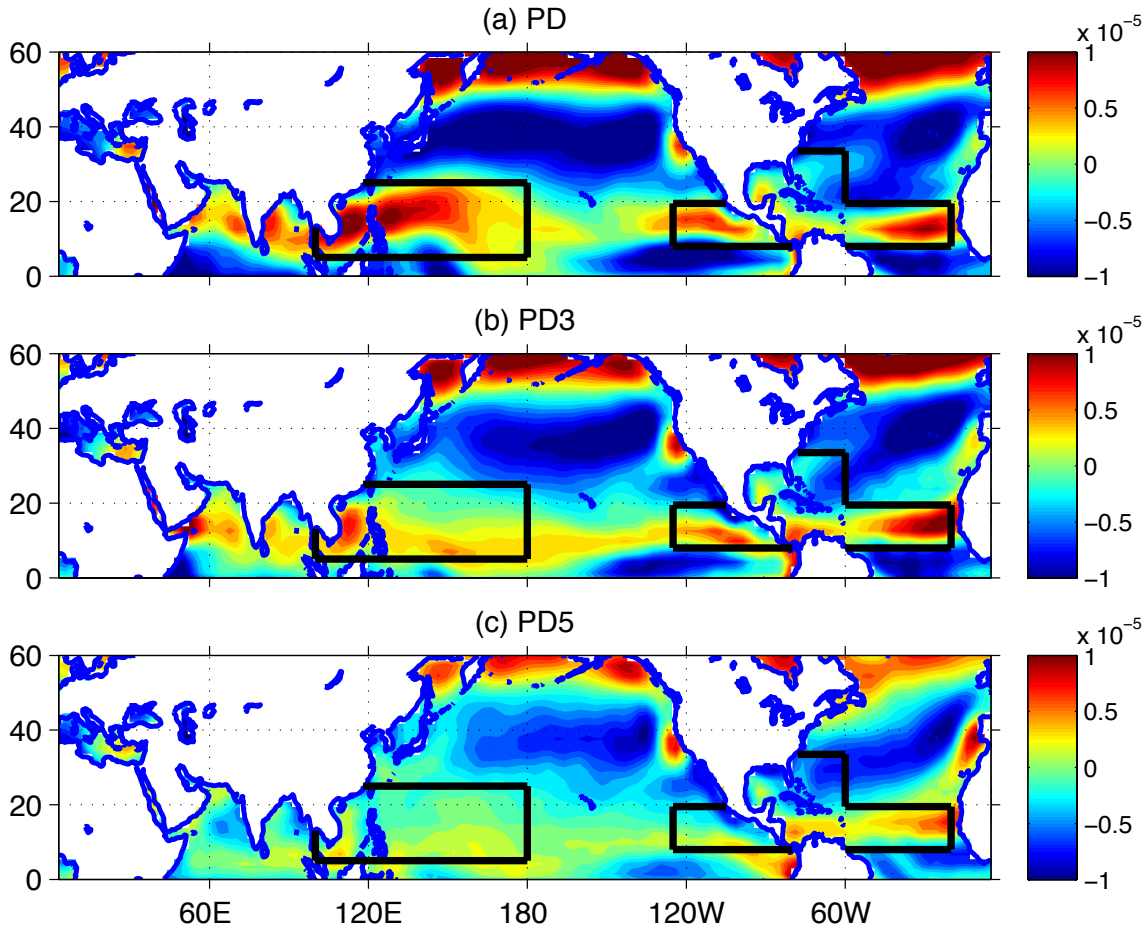

Figure 21: Relative vorticity (s^{-1}) in PD cases. Vorticity averaged over all Augusts, Septembers, and Octobers for (a) PD, (b) PD3, and (c) PD5 cases.

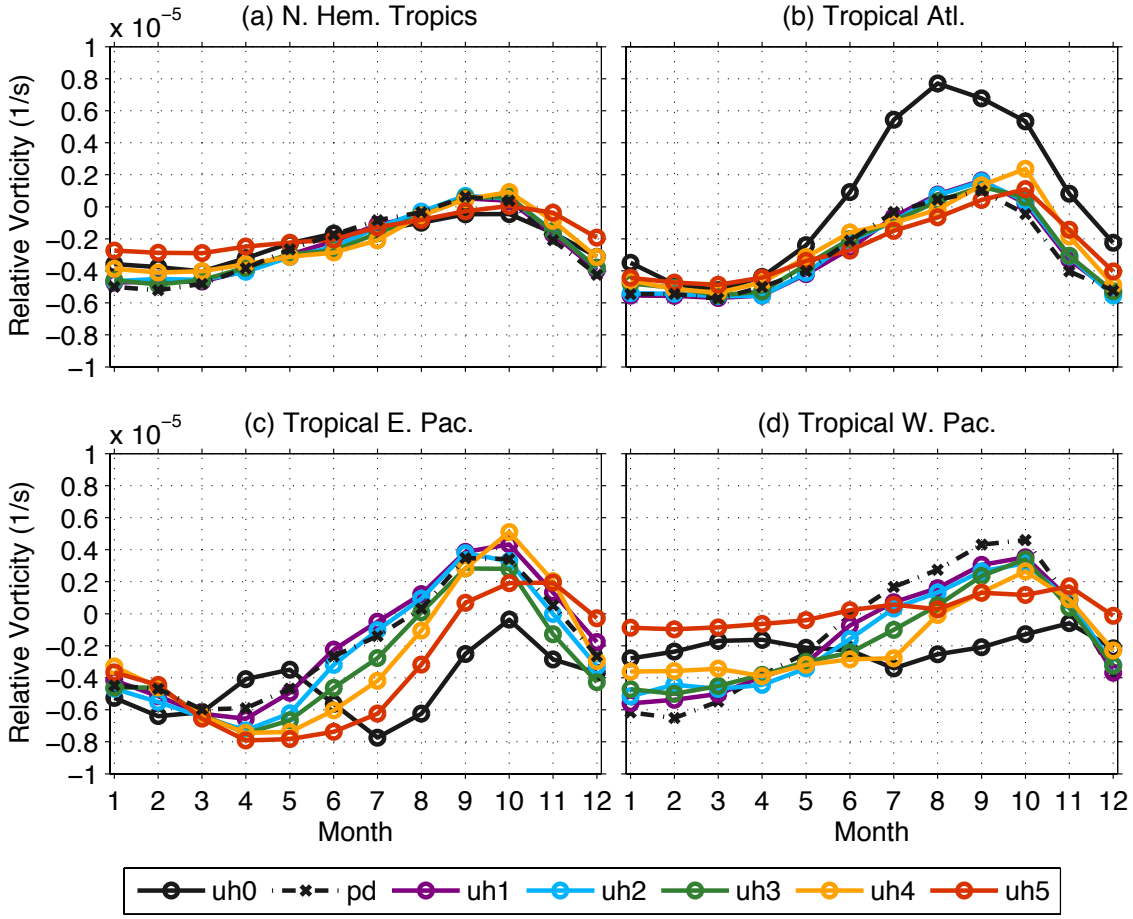

Figure 22: Annual cycle of relative vorticity. Vorticity averaged over (a) the Northern Hemisphere tropics, (b) Atlantic box, (c) Eastern Pacific box, and (d) Western Pacific box. Refer to Figure 1 and text for definition of areas.

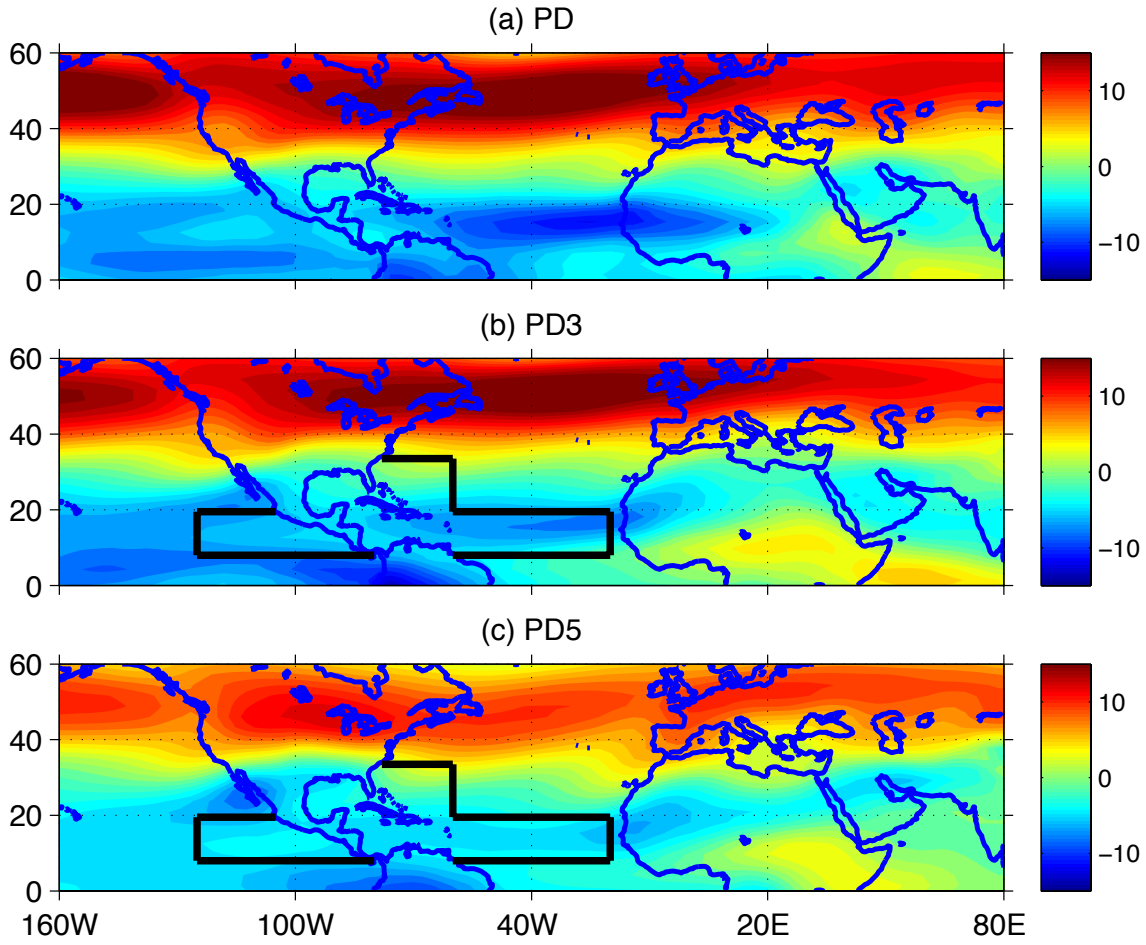

Figure 23: 700 mb zonal wind speed in PD cases. Wind speed (m/s) averaged over all Augusts, Septembers, and Octobers for (a) PD, (b) PD3, and (c) PD5 cases.

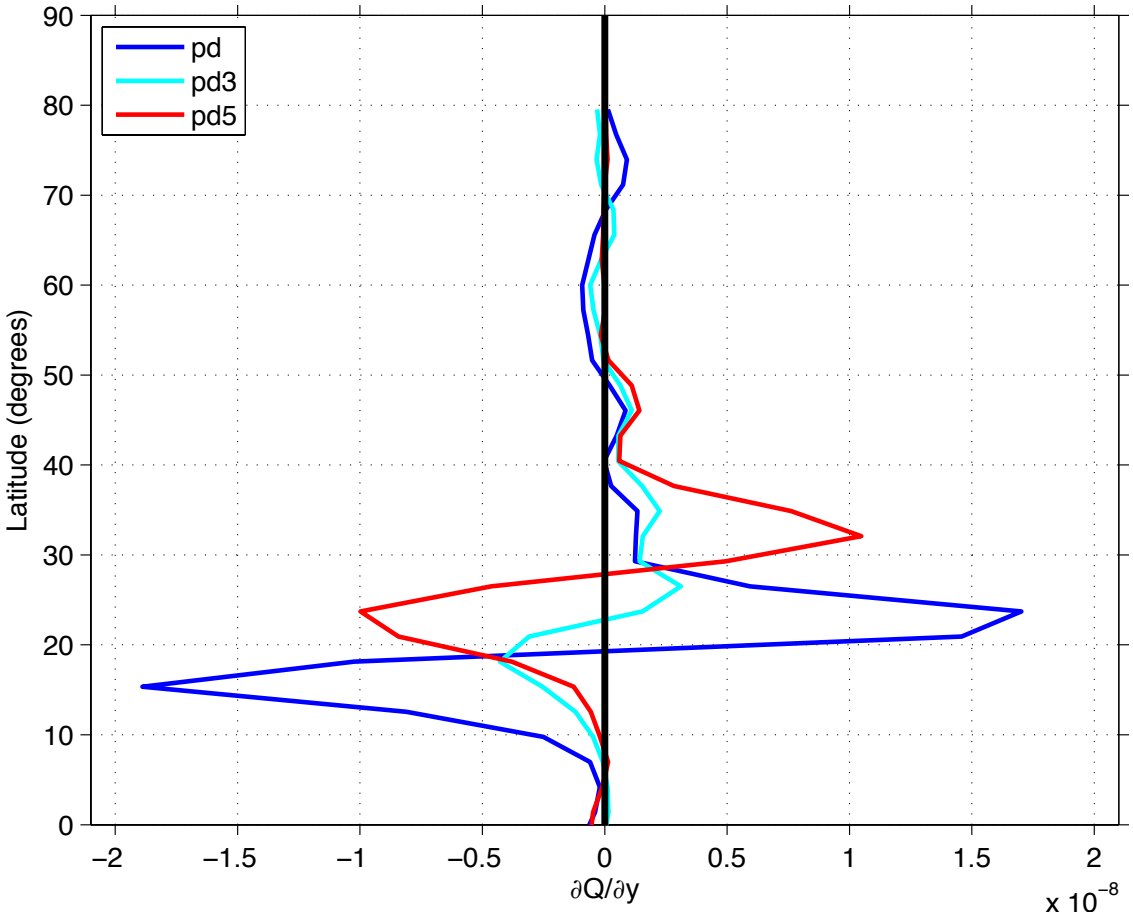

Figure 24: Meridional gradient of quasi-geostrophic potential vorticity. Time mean quasi-geostrophic potential vorticity taken along the prime meridian (units: $s^{-1}m^{-1}$).

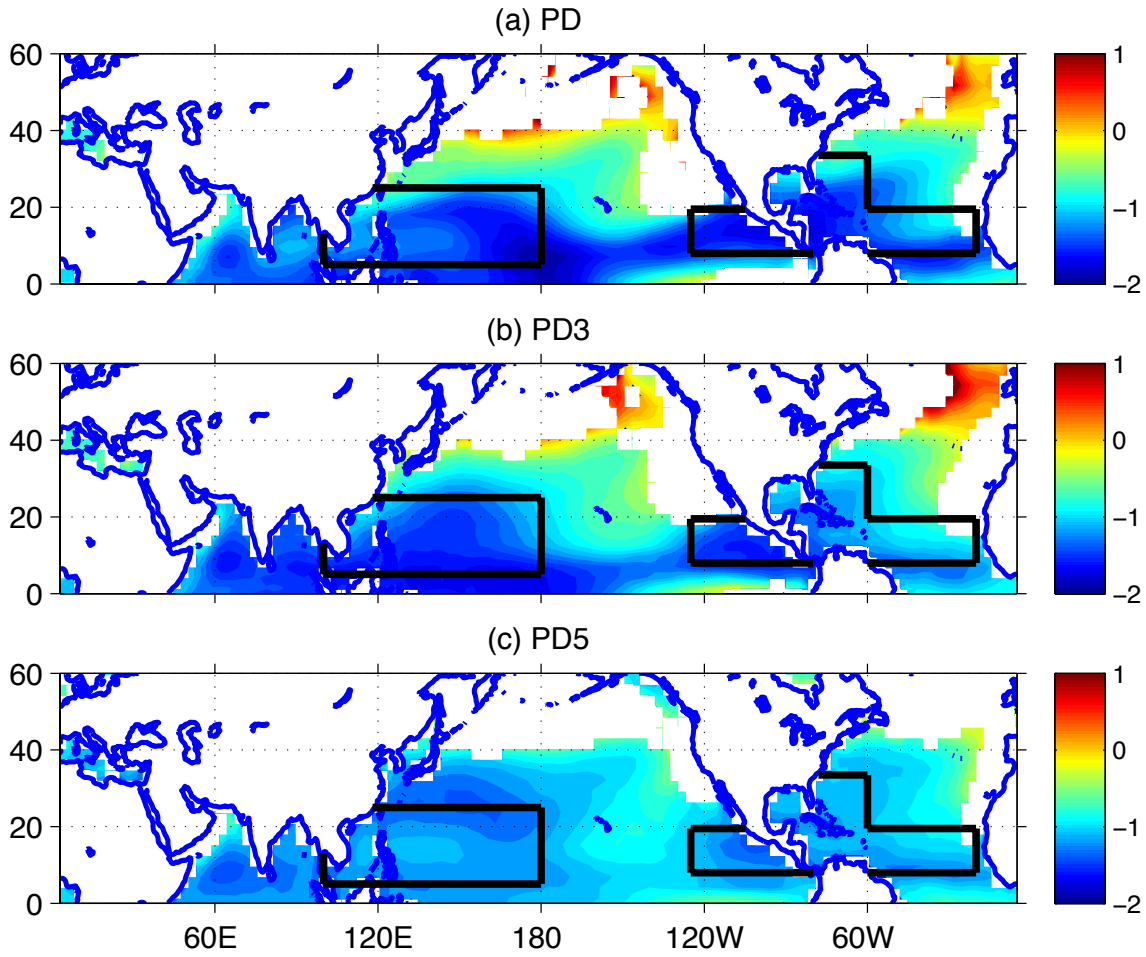

Figure 25: Non-dimensional incubation parameter γ in PD cases. γ averaged over all Augusts, Septembers, and Octobers for (a) PD, (b) PD3, and (c) PD5 cases. Values shown are $\log_{10}(\gamma)$.

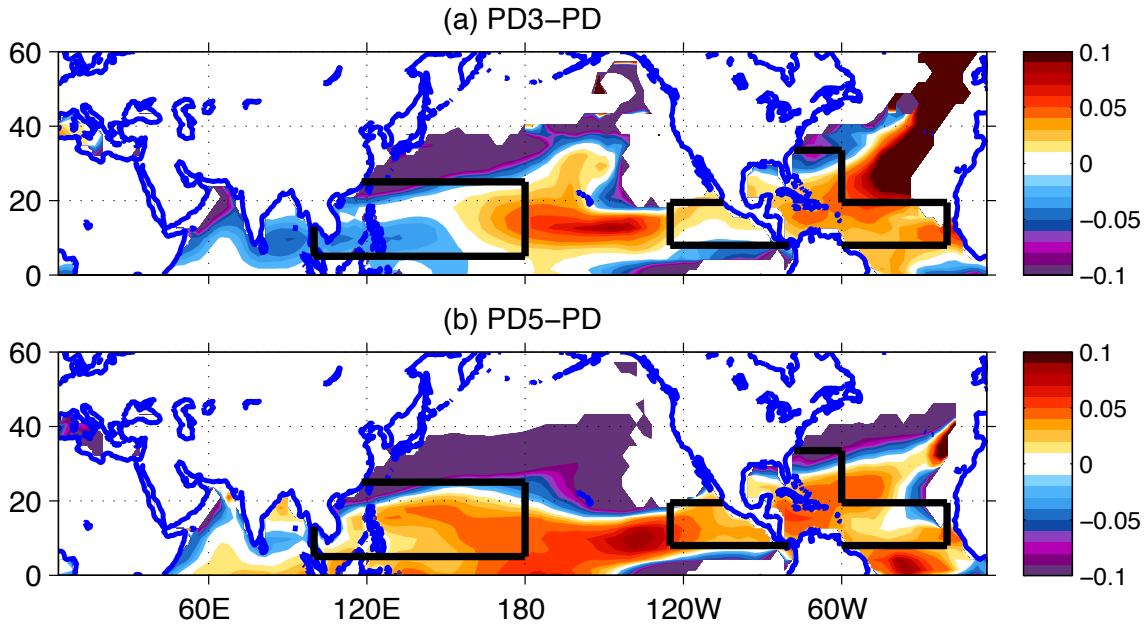

Figure 26: Change in γ. August-October Δγ between (a) PD3 and PD and (b) PD5 and PD.

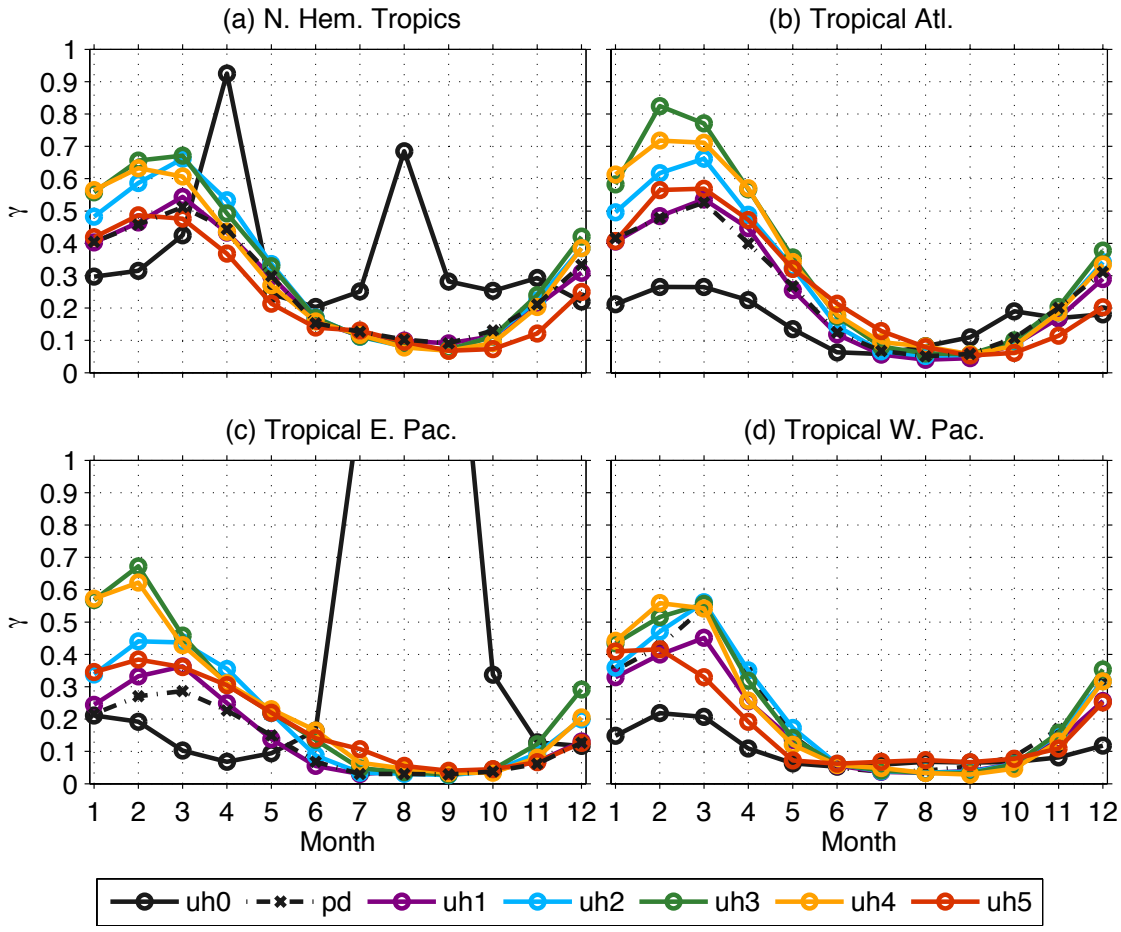

Figure 27: Annual cycle of γ. γ averaged over (a) the Northern Hemisphere tropics, (b) Atlantic box, (c) Eastern Pacific box, and (d) Western Pacific box. Refer to Figure 1 and text for definition of areas.

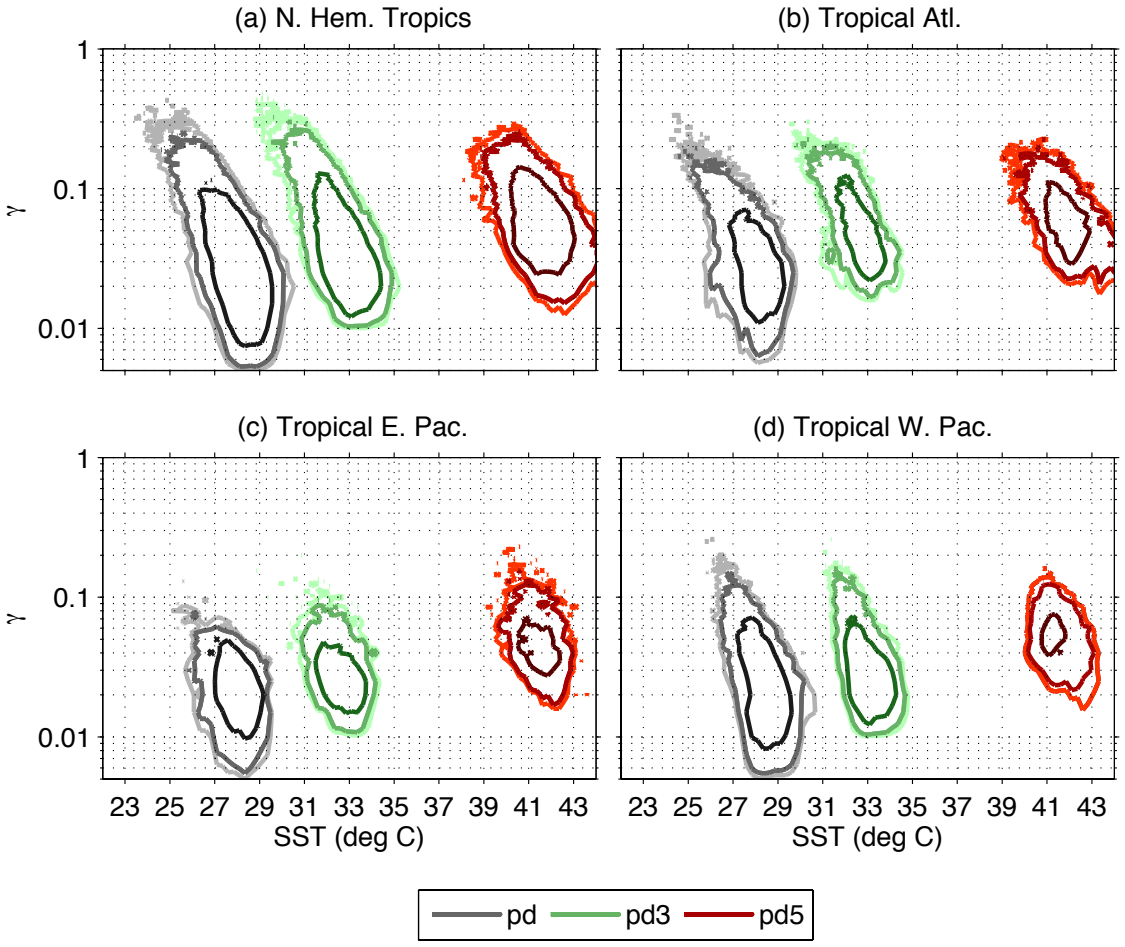

Figure 28: Joint distribution of SST and γ for PD cases. SST given in °C. Darker contours indicate higher densities.

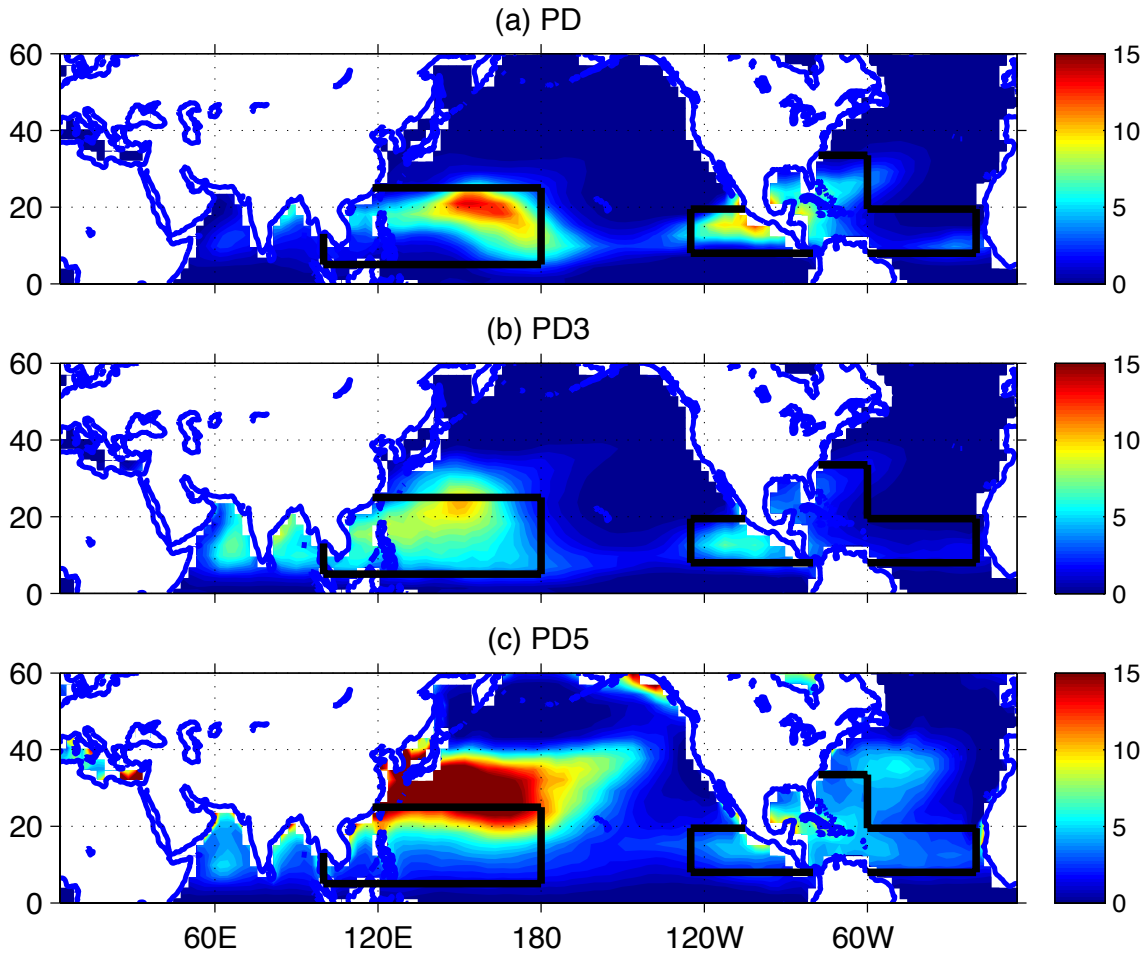

Figure 29: First form of the GPI (without AVL). GPI (Equation 1) averaged over all Augusts, Septembers, and Octobers for (a) PD, (b) PD3, and (c) PD5 cases. See Section 5b for definition of AVL.

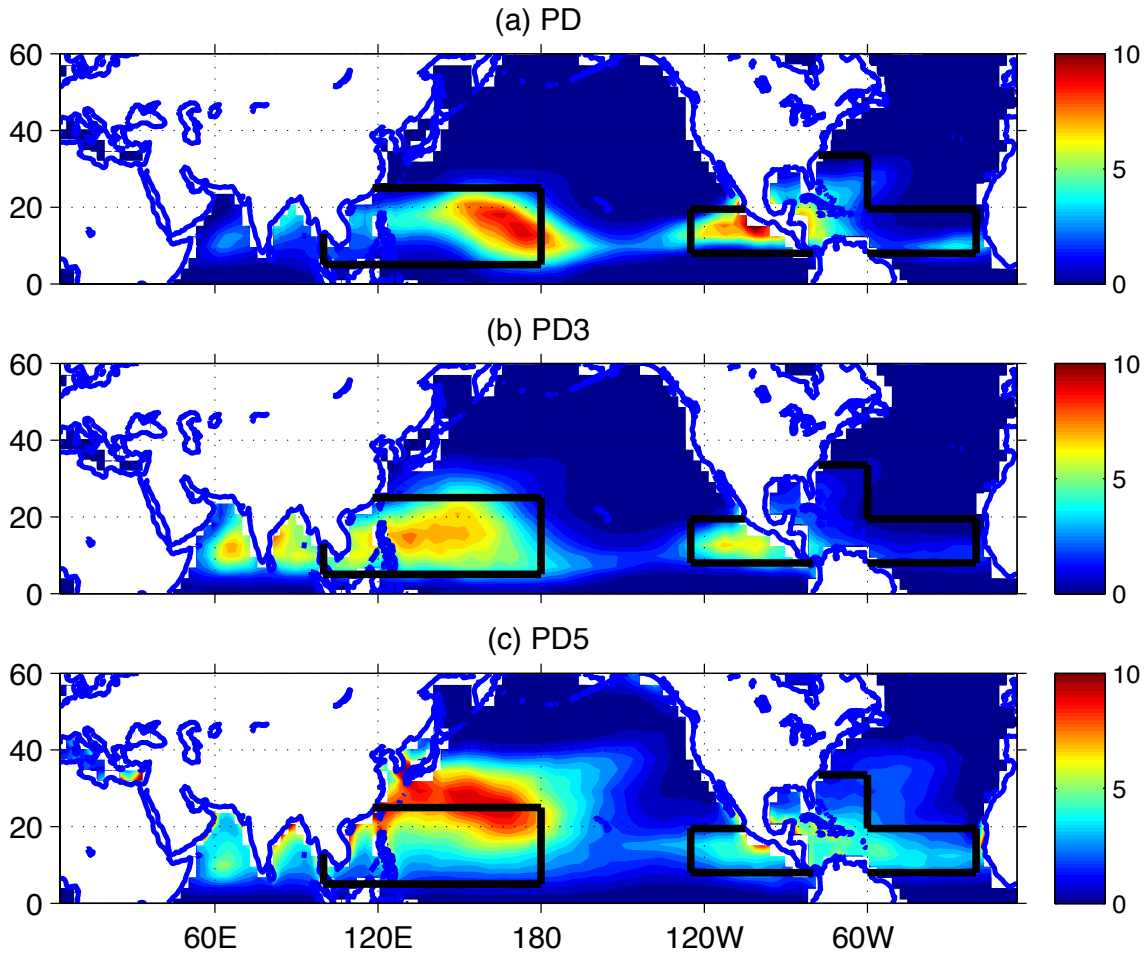

Figure 30: Modified first form of the GPI (includes AVL). GPI (Equation 1) averaged over all Augusts, Septembers, and Octobers for (a) PD, (b) PD3, and (c) PD5 cases. See Section 5b for definition of AVL.

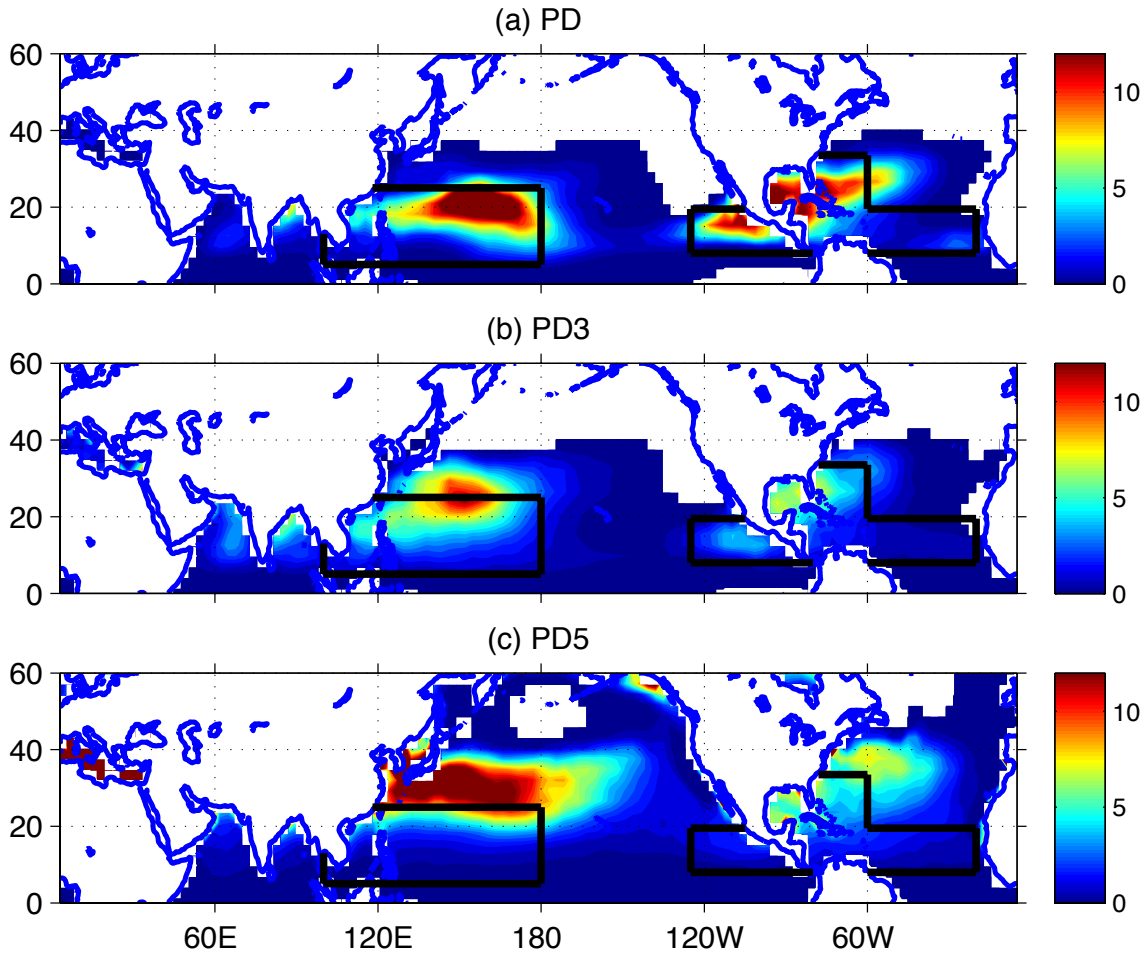

Figure 31: Second form of the GPI (without AVL). GPI (Equation 2) averaged over all Augusts, Septembers, and Octobers for (a) PD, (b) PD3, and (c) PD5 cases. See Section 5b for definition of AVL.

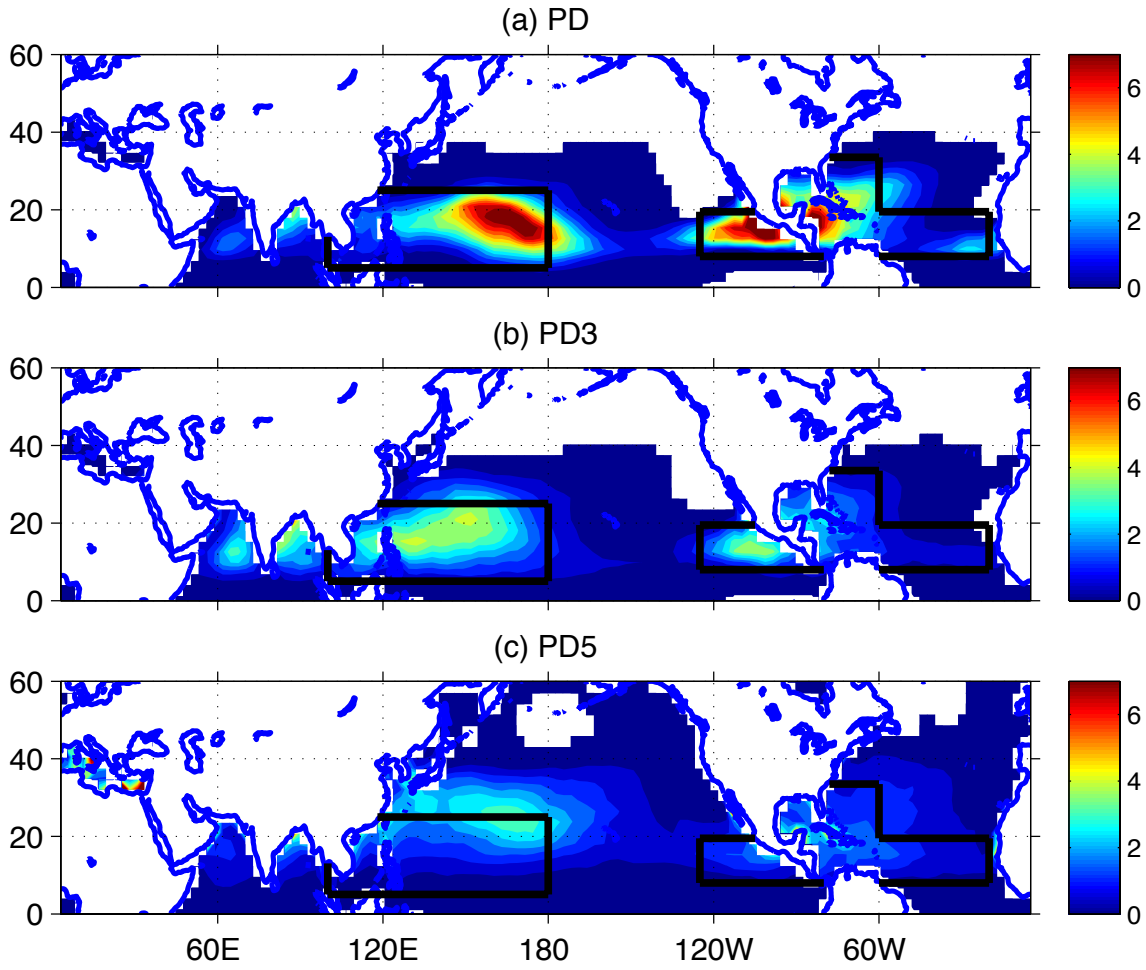

Figure 32: Modified second form of the GPI (includes AVL). GPI (Equation 2) averaged over all Augusts, Septembers, and Octobers for (a) PD, (b) PD3, and (c) PD5 cases. See Section 5b for definition of AVL.

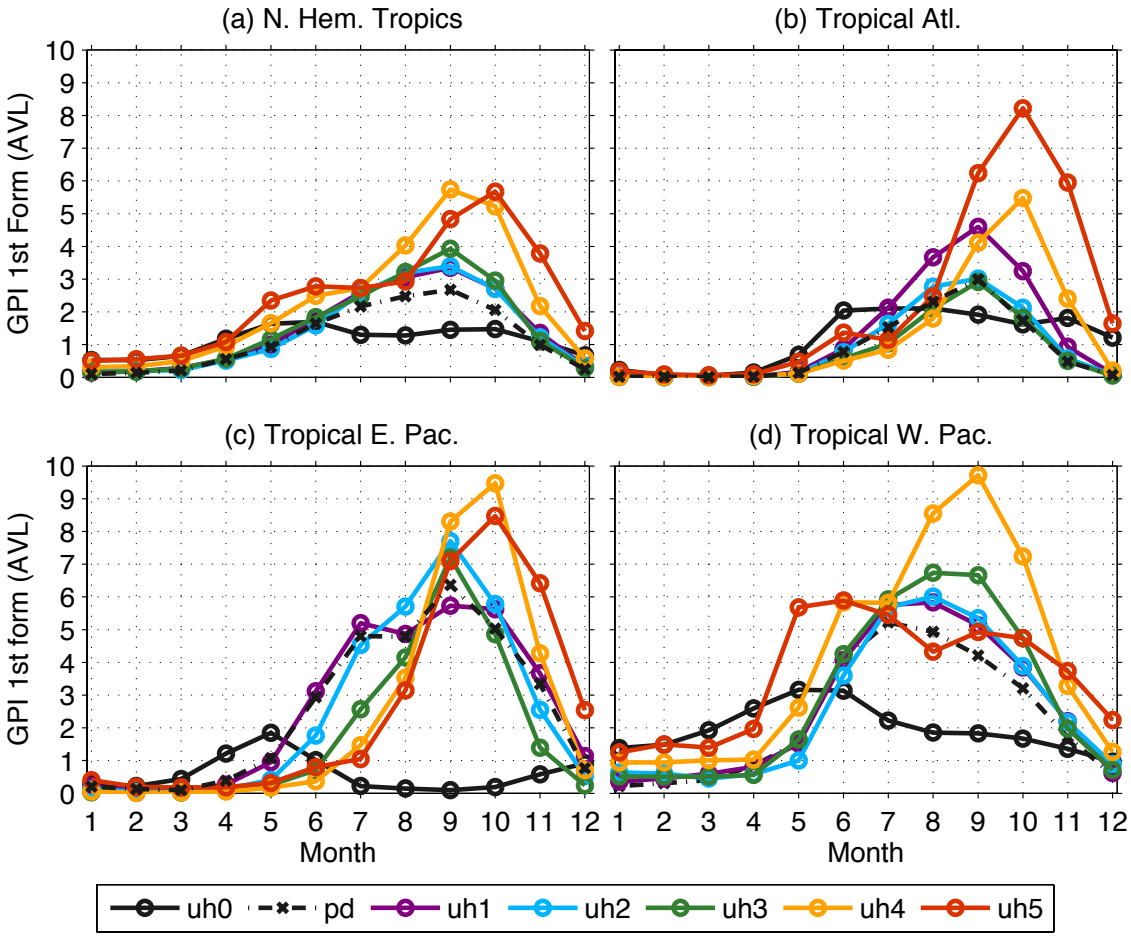

Figure 33: Annual cycle of GPI_1. GPI_1 averaged over (a) the Northern Hemisphere tropics, (b) Atlantic box, (c) Eastern Pacific box, and (d) Western Pacific box. Refer to Figure 1 and text for definition of areas.

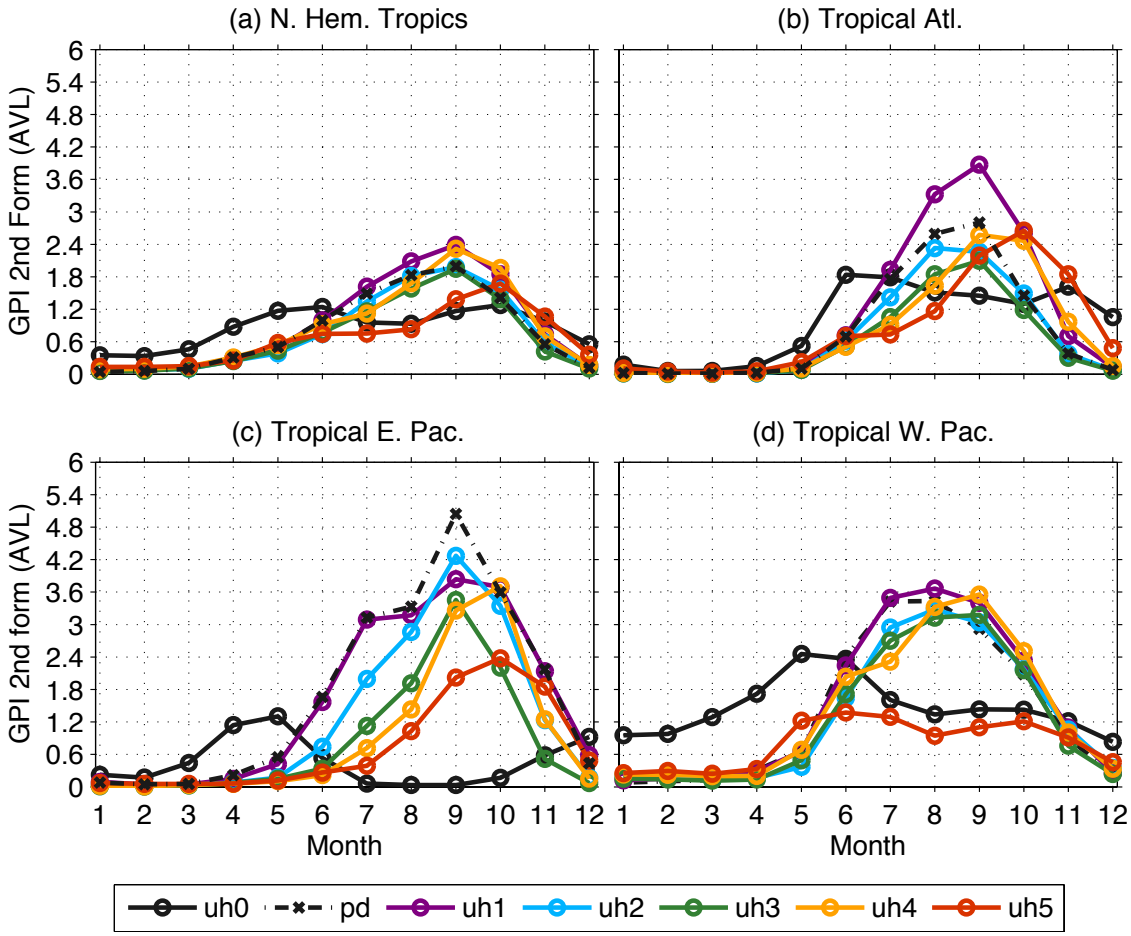

Figure 34: Annual cycle of GPI_2. GPI_2 averaged over (a) the Northern Hemisphere tropics, (b) Atlantic box, (c) Eastern Pacific box, and (d) Western Pacific box. Refer to Figure 1 and text for definition of areas.

VITA

Name:	Stephen Christopher Cathey
Address:	Stephen Cathey c/o Robert Korty Department of Atmospheric Sciences Texas A&M University College Station, TX 77843-3150
Email Address:	scathey81@hotmail.com
Education:	B.S., Mathematics, Texas Tech University, 2003 B.S., Atmospheric Sciences, Texas A&M University, 2008